EUROPEAN ORGANIZATION FOR NUCLEAR RESEARCH

CERN–EP/99–161

2 February 2000
Revised

A Precise Measurement of the τ Polarisation at LEP-1

DELPHI Collaboration

Abstract

The τ polarisation has been studied with the $e^+e^- \to \tau^+\tau^-$ data collected by the DELPHI detector at LEP in 1993, 1994 and 1995 around the Z resonance firstly through the exclusive decay channels $e\nu\bar{\nu}$, $\mu\nu\bar{\nu}$, $\pi\nu$, $\rho\nu$ and $a_1\nu$ and secondly with an inclusive hadronic analysis which benefits from a higher efficiency and a better systematic precision. The results have been combined with those previously published on 1990 to 1992 DELPHI data, to produce results which reflect the full LEP-1 statistics. The fit of the τ polarisation dependence on the production angle yielded the polarisation parameters $\mathcal{A}_\tau = 0.1359 \pm 0.0096$ and $\mathcal{A}_e = 0.1382 \pm 0.0116$. From these results the ratio of the vector and axial-vector effective couplings $\bar{v}_\tau/\bar{a}_\tau = 0.0683 \pm 0.0048$ and $\bar{v}_e/\bar{a}_e = 0.0694 \pm 0.0058$ have been derived, compatible with e$-\tau$ universality. With the assumption of lepton universality, the ratio of vector to axial-vector effective couplings for leptons $\bar{v}_l/\bar{a}_l = 0.0687 \pm 0.0037$ was obtained, implying a value of the effective weak mixing angle $\sin^2\theta^{\rm lept}_{\rm eff} = 0.23282 \pm 0.00092$.

(E. Phys. J. C14 (2000) 585)

P.Abreu[22], W.Adam[52], T.Adye[38], P.Adzic[12], I.Ajinenko[44], Z.Albrecht[18], T.Alderweireld[2], G.D.Alekseev[17], R.Alemany[51], T.Allmendinger[18], P.P.Allport[23], S.Almehed[25], U.Amaldi[9], N.Amapane[47], S.Amato[49], E.G.Anassontzis[3], P.Andersson[46], A.Andreazza[9], S.Andringa[22], P.Antilogus[26], W-D.Apel[18], Y.Arnoud[9], B.Åsman[46], J-E.Augustin[26], A.Augustinus[9], P.Baillon[9], P.Bambade[20], F.Barao[22], G.Barbiellini[48], R.Barbier[26], D.Y.Bardin[17], G.Barker[18], A.Baroncelli[40], M.Battaglia[16], M.Baubillier[24], K-H.Becks[54], M.Begalli[6], A.Behrmann[54], P.Beilliere[8], Yu.Belokopytov[9], N.C.Benekos[33], A.C.Benvenuti[5], C.Berat[15], M.Berggren[26], D.Bertini[26], D.Bertrand[2], M.Besancon[41], M.Bigi[47], M.S.Bilenky[17], M-A.Bizouard[20], D.Bloch[10], H.M.Blom[32], M.Bonesini[29], W.Bonivento[28], M.Boonekamp[41], P.S.L.Booth[23], A.W.Borgland[4], G.Borisov[20], C.Bosio[43], O.Botner[50], E.Boudinov[32], B.Bouquet[20], C.Bourdarios[20], T.J.V.Bowcock[23], I.Boyko[17], I.Bozovic[12], M.Bozzo[14], M.Bracko[45], P.Branchini[40], R.A.Brenner[50], P.Bruckman[9], J-M.Brunet[8], L.Bugge[34], T.Buran[34], B.Buschbeck[52], P.Buschmann[54], S.Cabrera[51], M.Caccia[28], M.Calvi[29], T.Camporesi[9], V.Canale[39], F.Carena[9], L.Carroll[23], C.Caso[14], M.V.Castillo Gimenez[51], A.Cattai[9], F.R.Cavallo[5], V.Chabaud[9], Ph.Charpentier[9], L.Chaussard[26], P.Checchia[37], G.A.Chelkov[17], R.Chierici[47], P.Chliapnikov[9,44], P.Chochula[7], V.Chorowicz[26], J.Chudoba[31], K.Cieslik[19], P.Collins[9], R.Contri[14], E.Cortina[51], G.Cosme[20], F.Cossutti[9], H.B.Crawley[1], D.Crennell[38], S.Crepe[15], G.Crosetti[14], J.Cuevas Maestro[35], S.Czellar[16], M.Davenport[9], W.Da Silva[24], G.Della Ricca[48], P.Delpierre[27], N.Demaria[9], A.De Angelis[48], W.De Boer[18], S.de Brabandere[2], C.De Clercq[2], B.De Lotto[48], A.De Min[37], L.De Paula[49], H.Dijkstra[9], L.Di Ciaccio[9,39], J.Dolbeau[8], K.Doroba[53], M.Dracos[10], J.Drees[54], M.Dris[33], A.Duperrin[26], J-D.Durand[9], G.Eigen[4], T.Ekelof[50], G.Ekspong[46], M.Ellert[50], M.Elsing[9], J-P.Engel[10], M.Espirito Santo[22], G.Fanourakis[12], D.Fassouliotis[12], J.Fayot[24], M.Feindt[18], A.Fenyuk[44], P.Ferrari[28], A.Ferrer[51], E.Ferrer-Ribas[20], F.Ferro[14], S.Fichet[24], A.Firestone[1], U.Flagmeyer[54], H.Foeth[9], E.Fokitis[33], F.Fontanelli[14], B.Franek[38], A.G.Frodesen[4], F.Fulda-Quenzer[20], J.Fuster[51], A.Galloni[23], D.Gamba[47], S.Gamblin[20], M.Gandelman[49], C.Garcia[51], C.Gaspar[9], M.Gaspar[49], U.Gasparini[37], Ph.Gavillet[9], E.N.Gazis[33], D.Gele[10], L.Gerdyukov[44], N.Ghodbane[26], I.Gil[51], F.Glege[54], R.Gokieli[9,53], B.Golob[9,45], G.Gomez-Ceballos[42], P.Goncalves[22], I.Gonzalez Caballero[42], G.Gopal[38], L.Gorn[1], Yu.Gouz[44], V.Gracco[14], J.Grahl[1], E.Graziani[40], P.Gris[41], G.Grosdidier[20], K.Grzelak[53], J.Guy[38], F.Hahn[9], S.Hahn[54], S.Haider[9], A.Hallgren[50], K.Hamacher[54], J.Hansen[34], F.J.Harris[36], V.Hedberg[9,25], S.Heising[18], J.J.Hernandez[51], P.Herquet[2], H.Herr[9], T.L.Hessing[36], J.-M.Heuser[54], E.Higon[51], S-O.Holmgren[46], P.J.Holt[36], S.Hoorelbeke[2], M.Houlden[23], J.Hrubec[52], M.Huber[18], K.Huet[2], G.J.Hughes[23], K.Hultqvist[9,46], J.N.Jackson[23], R.Jacobsson[9], P.Jalocha[19], R.Janik[7], Ch.Jarlskog[25], G.Jarlskog[25], P.Jarry[41], B.Jean-Marie[20], D.Jeans[36], E.K.Johansson[46], P.Jonsson[26], C.Joram[9], P.Juillot[10], L.Jungermann[18], F.Kapusta[24], K.Karafasoulis[12], S.Katsanevas[26], E.C.Katsoufis[33], R.Keranen[18], G.Kernel[45], B.P.Kersevan[45], B.A.Khomenko[17], N.N.Khovanski[17], A.Kiiskinen[16], B.King[23], A.Kinvig[23], N.J.Kjaer[9], O.Klapp[54], H.Klein[9], P.Kluit[32], P.Kokkinias[12], V.Kostioukhine[44], C.Kourkoumelis[3], O.Kouznetsov[41], M.Krammer[52], E.Kriznic[45], J.Krstic[12], Z.Krumstein[17], P.Kubinec[7], J.Kurowska[53], K.Kurvinen[16], J.W.Lamsa[1], D.W.Lane[1], V.Lapin[44], J-P.Laugier[41], R.Lauhakangas[16], G.Leder[52], F.Ledroit[15], V.Lefebure[2], L.Leinonen[46], A.Leisos[12], R.Leitner[31], G.Lenzen[54], V.Lepeltier[20], T.Lesiak[19], M.Lethuillier[41], J.Libby[36], W.Liebig[54], D.Liko[9], A.Lipniacka[9,46], I.Lippi[37], B.Loerstad[25], J.G.Loken[36], J.H.Lopes[49], J.M.Lopez[42], R.Lopez-Fernandez[15], D.Loukas[12], P.Lutz[41], L.Lyons[36], J.MacNaughton[52], J.R.Mahon[6], A.Maio[22], A.Malek[54], T.G.M.Malmgren[46], S.Maltezos[33], V.Malychev[17], F.Mandl[52], J.Marco[42], R.Marco[42], B.Marechal[49], M.Margoni[37], J-C.Marin[9], C.Mariotti[9], A.Markou[12], C.Martinez-Rivero[20], F.Martinez-Vidal[51], S.Marti i Garcia[9], J.Masik[13], N.Mastroyiannopoulos[12], F.Matorras[42], C.Matteuzzi[29], G.Matthiae[39], F.Mazzucato[37], M.Mazzucato[37], M.Mc Cubbin[23], R.Mc Kay[1], R.Mc Nulty[23], G.Mc Pherson[23], C.Meroni[28], W.T.Meyer[1], A.Miagkov[44], E.Migliore[9], L.Mirabito[26], W.A.Mitaroff[52], U.Mjoernmark[25], T.Moa[46], M.Moch[18], R.Moeller[30], K.Moenig[9,11], M.R.Monge[14], D.Moraes[49], X.Moreau[24], P.Morettini[14], G.Morton[36], U.Mueller[54], K.Muenich[54], M.Mulders[32], C.Mulet-Marquis[15], R.Muresan[25], W.J.Murray[38], B.Muryn[19], G.Myatt[36], T.Myklebust[34], F.Naraghi[15], M.Nassiakou[12], F.L.Navarria[5], S.Navas[51], K.Nawrocki[53], P.Negri[29], N.Neufeld[9], R.Nicolaidou[41], B.S.Nielsen[30], P.Niezurawski[53], M.Nikolenko[10,17], V.Nomokonov[16], A.Nygren[25], V.Obraztsov[44], A.G.Olshevski[17], A.Onofre[22], R.Orava[16], G.Orazi[10], K.Osterberg[16], A.Ouraou[41], M.Paganoni[29], S.Paiano[5], R.Pain[24], R.Paiva[22], J.Palacios[36], H.Palka[19], Th.D.Papadopoulou[9,33], K.Papageorgiou[12], L.Pape[9], C.Parkes[9], F.Parodi[14], U.Parzefall[23], A.Passeri[40], O.Passon[54], T.Pavel[25], M.Pegoraro[37], L.Peralta[22], M.Pernicka[52], A.Perrotta[5], C.Petridou[48], A.Petrolini[14], H.T.Phillips[38], F.Pierre[41], M.Pimenta[22], E.Piotto[28], T.Podobnik[45], M.E.Pol[6], G.Polok[19], E.Polycarpo[49], P.Poropat[48], V.Pozdniakov[17], P.Privitera[39], N.Pukhaeva[17], A.Pullia[29], D.Radojicic[36], S.Ragazzi[29], H.Rahmani[33], J.Rames[13], P.N.Ratoff[21], A.L.Read[34], P.Rebecchi[9], N.G.Redaelli[28], M.Regler[52], J.Rehn[18], D.Reid[32], R.Reinhardt[54], P.B.Renton[36], L.K.Resvanis[3], F.Richard[20], J.Ridky[13], G.Rinaudo[47], I.Ripp-Baudot[10], O.Rohne[34], A.Romero[47], P.Ronchese[37], E.I.Rosenberg[1], P.Rosinsky[7], P.Roudeau[20], T.Rovelli[5], Ch.Royon[41], V.Ruhlmann-Kleider[41], A.Ruiz[42], H.Saarikko[16], Y.Sacquin[41], A.Sadovsky[17], G.Sajot[15], J.Salt[51], D.Sampsonidis[12], M.Sannino[14], Ph.Schwemling[24], B.Schwering[54], U.Schwickerath[18], F.Scuri[48], P.Seager[21], Y.Sedykh[17], A.M.Segar[36], N.Seibert[18], R.Sekulin[38], R.C.Shellard[6], M.Siebel[54], L.Simard[41], F.Simonetto[37], A.N.Sisakian[17], G.Smadja[26], N.Smirnov[44], O.Smirnova[25], G.R.Smith[38], A.Sopczak[18], R.Sosnowski[53], T.Spassov[22], E.Spiriti[40], S.Squarcia[14], C.Stanescu[40], S.Stanic[45], M.Stanitzki[18], K.Stevenson[36], A.Stocchi[20], J.Strauss[52], R.Strub[10], B.Stugu[4], M.Szczekowski[53], M.Szeptycka[53], T.Tabarelli[29], A.Taffard[23], F.Tegenfeldt[50], F.Terranova[29], J.Thomas[36], J.Timmermans[32], N.Tinti[5], L.G.Tkatchev[17], M.Tobin[23], S.Todorova[10], A.Tomaradze[2], B.Tome[22], A.Tonazzo[9],

L.Tortora[40], P.Tortosa[51], G.Transtromer[25], D.Treille[9], G.Tristram[8], M.Trochimczuk[53], C.Troncon[28], M-L.Turluer[41], I.A.Tyapkin[17], S.Tzamarias[12], O.Ullaland[9], V.Uvarov[44], G.Valenti[9,5], E.Vallazza[48], P.Van Dam[32], W.Van den Boeck[2], W.K.Van Doninck[2], J.Van Eldik[9,32], A.Van Lysebetten[2], N.van Remortel[2], I.Van Vulpen[32], G.Vegni[28], L.Ventura[37], W.Venus[38,9], F.Verbeure[2], M.Verlato[37], L.S.Vertogradov[17], V.Verzi[39], D.Vilanova[41], L.Vitale[48], E.Vlasov[44], A.S.Vodopyanov[17], G.Voulgaris[3], V.Vrba[13], H.Wahlen[54], C.Walck[46], A.J.Washbrook[23], C.Weiser[9], D.Wicke[54], J.H.Wickens[2], G.R.Wilkinson[36], M.Winter[10], M.Witek[19], G.Wolf[9], J.Yi[1], O.Yushchenko[44], A.Zalewska[19], P.Zalewski[53], D.Zavrtanik[45], E.Zevgolatakos[12], N.I.Zimin[17,25], A.Zintchenko[17], Ph.Zoller[10], G.C.Zucchelli[46], G.Zumerle[37]

[1] Department of Physics and Astronomy, Iowa State University, Ames IA 50011-3160, USA
[2] Physics Department, Univ. Instelling Antwerpen, Universiteitsplein 1, B-2610 Antwerpen, Belgium
and IIHE, ULB-VUB, Pleinlaan 2, B-1050 Brussels, Belgium
and Faculté des Sciences, Univ. de l'Etat Mons, Av. Maistriau 19, B-7000 Mons, Belgium
[3] Physics Laboratory, University of Athens, Solonos Str. 104, GR-10680 Athens, Greece
[4] Department of Physics, University of Bergen, Allégaten 55, NO-5007 Bergen, Norway
[5] Dipartimento di Fisica, Università di Bologna and INFN, Via Irnerio 46, IT-40126 Bologna, Italy
[6] Centro Brasileiro de Pesquisas Físicas, rua Xavier Sigaud 150, BR-22290 Rio de Janeiro, Brazil
and Depto. de Física, Pont. Univ. Católica, C.P. 38071 BR-22453 Rio de Janeiro, Brazil
and Inst. de Física, Univ. Estadual do Rio de Janeiro, rua São Francisco Xavier 524, Rio de Janeiro, Brazil
[7] Comenius University, Faculty of Mathematics and Physics, Mlynska Dolina, SK-84215 Bratislava, Slovakia
[8] Collège de France, Lab. de Physique Corpusculaire, IN2P3-CNRS, FR-75231 Paris Cedex 05, France
[9] CERN, CH-1211 Geneva 23, Switzerland
[10] Institut de Recherches Subatomiques, IN2P3 - CNRS/ULP - BP20, FR-67037 Strasbourg Cedex, France
[11] Now at DESY-Zeuthen, Platanenallee 6, D-15735 Zeuthen, Germany
[12] Institute of Nuclear Physics, N.C.S.R. Demokritos, P.O. Box 60228, GR-15310 Athens, Greece
[13] FZU, Inst. of Phys. of the C.A.S. High Energy Physics Division, Na Slovance 2, CZ-180 40, Praha 8, Czech Republic
[14] Dipartimento di Fisica, Università di Genova and INFN, Via Dodecaneso 33, IT-16146 Genova, Italy
[15] Institut des Sciences Nucléaires, IN2P3-CNRS, Université de Grenoble 1, FR-38026 Grenoble Cedex, France
[16] Helsinki Institute of Physics, HIP, P.O. Box 9, FI-00014 Helsinki, Finland
[17] Joint Institute for Nuclear Research, Dubna, Head Post Office, P.O. Box 79, RU-101 000 Moscow, Russian Federation
[18] Institut für Experimentelle Kernphysik, Universität Karlsruhe, Postfach 6980, DE-76128 Karlsruhe, Germany
[19] Institute of Nuclear Physics and University of Mining and Metalurgy, Ul. Kawiory 26a, PL-30055 Krakow, Poland
[20] Université de Paris-Sud, Lab. de l'Accélérateur Linéaire, IN2P3-CNRS, Bât. 200, FR-91405 Orsay Cedex, France
[21] School of Physics and Chemistry, University of Lancaster, Lancaster LA1 4YB, UK
[22] LIP, IST, FCUL - Av. Elias Garcia, 14-1°, PT-1000 Lisboa Codex, Portugal
[23] Department of Physics, University of Liverpool, P.O. Box 147, Liverpool L69 3BX, UK
[24] LPNHE, IN2P3-CNRS, Univ. Paris VI et VII, Tour 33 (RdC), 4 place Jussieu, FR-75252 Paris Cedex 05, France
[25] Department of Physics, University of Lund, Sölvegatan 14, SE-223 63 Lund, Sweden
[26] Université Claude Bernard de Lyon, IPNL, IN2P3-CNRS, FR-69622 Villeurbanne Cedex, France
[27] Univ. d'Aix - Marseille II - CPP, IN2P3-CNRS, FR-13288 Marseille Cedex 09, France
[28] Dipartimento di Fisica, Università di Milano and INFN, Via Celoria 16, IT-20133 Milan, Italy
[29] Università degli Studi di Milano - Bicocca, Via Emanuelli 15, IT-20126 Milan, Italy
[30] Niels Bohr Institute, Blegdamsvej 17, DK-2100 Copenhagen Ø, Denmark
[31] IPNP of MFF, Charles Univ., Areal MFF, V Holesovickach 2, CZ-180 00, Praha 8, Czech Republic
[32] NIKHEF, Postbus 41882, NL-1009 DB Amsterdam, The Netherlands
[33] National Technical University, Physics Department, Zografou Campus, GR-15773 Athens, Greece
[34] Physics Department, University of Oslo, Blindern, NO-1000 Oslo 3, Norway
[35] Dpto. Fisica, Univ. Oviedo, Avda. Calvo Sotelo s/n, ES-33007 Oviedo, Spain
[36] Department of Physics, University of Oxford, Keble Road, Oxford OX1 3RH, UK
[37] Dipartimento di Fisica, Università di Padova and INFN, Via Marzolo 8, IT-35131 Padua, Italy
[38] Rutherford Appleton Laboratory, Chilton, Didcot OX11 OQX, UK
[39] Dipartimento di Fisica, Università di Roma II and INFN, Tor Vergata, IT-00173 Rome, Italy
[40] Dipartimento di Fisica, Università di Roma III and INFN, Via della Vasca Navale 84, IT-00146 Rome, Italy
[41] DAPNIA/Service de Physique des Particules, CEA-Saclay, FR-91191 Gif-sur-Yvette Cedex, France
[42] Instituto de Fisica de Cantabria (CSIC-UC), Avda. los Castros s/n, ES-39006 Santander, Spain
[43] Dipartimento di Fisica, Università degli Studi di Roma La Sapienza, Piazzale Aldo Moro 2, IT-00185 Rome, Italy
[44] Inst. for High Energy Physics, Serpukov P.O. Box 35, Protvino, (Moscow Region), Russian Federation
[45] J. Stefan Institute, Jamova 39, SI-1000 Ljubljana, Slovenia and Laboratory for Astroparticle Physics,
Nova Gorica Polytechnic, Kostanjeviska 16a, SI-5000 Nova Gorica, Slovenia,
and Department of Physics, University of Ljubljana, SI-1000 Ljubljana, Slovenia
[46] Fysikum, Stockholm University, Box 6730, SE-113 85 Stockholm, Sweden
[47] Dipartimento di Fisica Sperimentale, Università di Torino and INFN, Via P. Giuria 1, IT-10125 Turin, Italy
[48] Dipartimento di Fisica, Università di Trieste and INFN, Via A. Valerio 2, IT-34127 Trieste, Italy
and Istituto di Fisica, Università di Udine, IT-33100 Udine, Italy
[49] Univ. Federal do Rio de Janeiro, C.P. 68528 Cidade Univ., Ilha do Fundão BR-21945-970 Rio de Janeiro, Brazil
[50] Department of Radiation Sciences, University of Uppsala, P.O. Box 535, SE-751 21 Uppsala, Sweden
[51] IFIC, Valencia-CSIC, and D.F.A.M.N., U. de Valencia, Avda. Dr. Moliner 50, ES-46100 Burjassot (Valencia), Spain
[52] Institut für Hochenergiephysik, Österr. Akad. d. Wissensch., Nikolsdorfergasse 18, AT-1050 Vienna, Austria
[53] Inst. Nuclear Studies and University of Warsaw, Ul. Hoza 69, PL-00681 Warsaw, Poland
[54] Fachbereich Physik, University of Wuppertal, Postfach 100 127, DE-42097 Wuppertal, Germany

1 Introduction

During the first phase of operation of LEP, the Large Electron Positron collider at CERN, electrons and positrons collided at a centre-of-mass energy around the Z mass, the dominant process being the e^+e^- annihilation into a Z boson. This reaction and the subsequent Z decay to fermion pairs takes place through the weak interaction which is parity violating. One of the most interesting effects of this parity violation is the existence of a non-zero average polarisation of the Z and of the final state fermion-antifermion pair. The τ weak decay within the detector provides a unique possibility to measure this polarisation.

In the absence of beam longitudinal polarisation, as was the case at LEP, the average polarisation of the Z is given in the improved Born approximation neglecting the γ exchange, the $\gamma - \mathrm{Z}$ interference and assuming $E_{cm} = M_{\mathrm{Z}}$ by [1]

$$\mathcal{P}_{\mathrm{z}} = -\frac{2\bar{a}_{\mathrm{e}}\bar{v}_{\mathrm{e}}}{\bar{a}_{\mathrm{e}}^2 + \bar{v}_{\mathrm{e}}^2} \equiv -\mathcal{A}_{\mathrm{e}}, \tag{1}$$

where $\bar{v}_{\mathrm{e}}$ and $\bar{a}_{\mathrm{e}}$ are respectively the vector and axial-vector effective couplings of the electron to the Z. The polarisation of the τ, $\langle\mathcal{P}_\tau\rangle$, averaged over the full solid angle is

$$\langle\mathcal{P}_\tau\rangle = -\frac{2\bar{a}_\tau\bar{v}_\tau}{\bar{a}_\tau^2 + \bar{v}_\tau^2} \equiv -\mathcal{A}_\tau, \tag{2}$$

where $\bar{v}_\tau$ and $\bar{a}_\tau$ are respectively the vector and axial-vector effective couplings of the τ to the Z. The positive and negative taus are produced with opposite polarisations.

The polarisation of the Z induces a dependence of $\mathcal{P}_\tau$ on the polar angle Θ, defined as the angle of the outgoing τ^- with respect to the incident e^- beam. At the Born level, this has the form

$$\mathcal{P}_\tau(\cos\Theta) = \frac{\langle\mathcal{P}_\tau\rangle \cdot (1+\cos^2\Theta) + \mathcal{P}_{\mathrm{z}} \cdot 2\cos\Theta}{(1+\cos^2\Theta) + \frac{4}{3}A_{FB} \cdot 2\cos\Theta}. \tag{3}$$

where A_{FB} is the forward-backward charge asymmetry of τ production.

Therefore with the study of the τ polarisation as a function of the polar angle it is possible to investigate both the $\mathrm{Z}\tau\tau$ and the $\mathrm{Z}ee$ couplings. In this paper we will assume the V$-$A structure of the weak charged current (several experimental results support this assumption in tau decays [2]). A DELPHI measurement of $\mathcal{P}_\tau$ without this assumption can be found in [3]. Several studies from DELPHI [4,5] and other LEP collaborations [6] have proved the feasibility of this procedure. With this measurement the ratios of the effective couplings $\bar{v}_{\mathrm{e}}/\bar{a}_{\mathrm{e}}$ and $\bar{v}_\tau/\bar{a}_\tau$ can each be obtained, allowing a test of e$-\tau$ universality. Furthermore, this measurement removes the sign ambiguity present in the measurements of forward-backward charge asymmetries where only the absolute value of the ratio of the couplings is accessible. Finally, an estimate of the effective weak mixing parameter for leptons, $\sin^2\theta_{\mathrm{eff}}^{\mathrm{lept}}$, can be derived from the relation $\bar{v}_l/\bar{a}_l = 1 - 4\sin^2\theta_{\mathrm{eff}}^{\mathrm{lept}}$, l =e, τ. This can be compared with results obtained from other measurements to test the validity of the Standard Model.

The radiative corrections, centre-of-mass energy dependence, γ exchange contribution and $\gamma - \mathrm{Z}$ interference modify the above expressions to a non-negligible level, considering the precisions achieved in this analysis. This is discussed in Section 9 where a new and more precise approach for obtaining the couplings is discussed.

The results and description given in Sections 3 to 8 are based on a sample of $\mathrm{Z} \to \tau^+\tau^-$ events observed in the DELPHI detector in 1993, 1994 and 1995 corresponding to an

integrated luminosity of 109.8 pb^{-1} at centre-of-mass energies close to the Z mass. In Section 9, these results are combined with the analysis of the 1990-1992 data, published in [5], in order to give results of the DELPHI experiment for the full LEP-1 data set. The 1990 data [4] were combined only after integrating over the production angle. The analysis is extended to the polar angle range $|\cos\Theta| < 0.94$, although for some decay channels it was restricted to the barrel section of the DELPHI detector, $|\cos\Theta| < 0.73$, to optimise the signal to background ratio.

The τ decay channels used and methods followed to extract the polarisation are very similar to those in [5]:

- $e\nu\bar{\nu}$, using a momentum estimator based on both charged particle momentum and calorimetric energy measurements;
- $\mu\nu\bar{\nu}$, using the μ momentum spectrum;
- $\pi\nu$ and $K\nu$, using the momentum spectrum of the π/K's, where no attempt is made at $\pi-$K separation;
- $\rho\nu$, using the variable ξ described in [7], constructed from various decay angles and the $\pi\pi$ invariant mass;
- $a_1\nu$, where the a_1 decays to three charged π's, using moments of various angular distributions sensitive to the τ polarisation [8];
- inclusive hadron, where all one prong hadronic channels are included with no attempt to separate them and with similar estimators to the π and ρ cases.

The main differences with respect to [5] are the extension in polar angle range of the muon and inclusive analyses as well as the inclusion of a neural network based analysis of all the one prong decays. This optimises the channel separation, includes the new channel $a_1 \to \pi 2\pi^0$ and allows a global fit to the polarisation and branching ratios.

The different techniques used to estimate the τ polarisation are discussed in Section 2. The DELPHI detector is described in Section 3 and its particle identification capabilities in Section 4. The data sample of $e^+e^- \to \tau^+\tau^-$ events used in the analysis is outlined in Section 5. The analyses of the exclusive decay modes and the inclusive hadronic one-prong analysis are described in Sections 6 and 7 respectively, while the neural network analysis is described in Section 8. The combination of the results from the different analyses is discussed in Section 9 and a summary of the measurements is provided in Section 10.

2 Techniques used for τ polarisation determination

The τ polarisation is reflected in the angular distributions of its decay products in the τ rest frame. The angular distribution affects the momenta of the final state particles in the laboratory frame, which can thus be used to infer the τ polarisation.

In the case of a leptonic decay, the only information available to determine the τ polarisation lies in the shape of the momentum spectrum. Ignoring mass effects, at Born level this has the form [1]

$$\frac{1}{N}\frac{dN}{dx} = \frac{1}{3}[(5 - 9x^2 + 4x^3) + \mathcal{P}_\tau(1 - 9x^2 + 8x^3)], \tag{4}$$

where x is the lepton energy divided by the τ energy. The analysis took account of mass effects and higher order corrections.

For a hadronic decay $\tau \to h\nu$ the polar angle, θ_h, distribution of the hadronic system h with respect to the τ direction in the τ rest frame has the form

$$\frac{1}{N}\frac{dN}{d\cos\theta_h} = \frac{1}{2}(1 + \alpha\mathcal{P}_\tau \cos\theta_h). \tag{5}$$

The angle θ_h can be approximately calculated from the laboratory momentum of the hadronic system p_h via the relation

$$\cos\theta_h \approx \frac{\frac{2p_h}{p_\tau} - 1 - \frac{m_h^2}{m_\tau^2}}{1 - \frac{m_h^2}{m_\tau^2}}, \tag{6}$$

where m_h is the mass of the hadronic system and p_τ and m_τ are the momentum and mass of the τ respectively. For a decay containing a spin-0 hadron such as $\pi\nu$ or Kν the constant α is unity. These decays retain the maximum sensitivity to $\mathcal{P}_\tau$.

In decays of the τ to spin-1 particles, the possibility of several polarisation states of the spin-1 particle reduces the sensitivity of the momentum spectrum, the constant α having the form

$$\alpha = \frac{m_\tau^2 - 2m_h^2}{m_\tau^2 + 2m_h^2}. \tag{7}$$

Defining the sensitivity of a given channel as the average precision achieved per τ decay relative to that for the $\pi\nu$ decay, the above expression results in a value of about 0.46 for the $\rho\nu$ and 0.12 for the $a_1\nu$ decay. The sensitivity can be improved by including information from the decay of the hadronic system. The extraction of the τ polarisation therefore involves a multidimensional distribution, which can be written in the general form

$$W(\vec{x}) = f(\vec{x}) + \mathcal{P}_\tau g(\vec{x}), \tag{8}$$

with $\vec{x}$ representing the set of variables used. These variables are typically functions of the angles between, and the momenta of, the final state particles. It has been shown [7] that with no loss of information the fitting is simplified considerably by using the one-dimensional distribution

$$\widehat{W}(\xi) = \hat{f}(\xi)[1 + \mathcal{P}_\tau \xi], \tag{9}$$

where ξ is defined as $\xi = g(\vec{x})/f(\vec{x})$.

This approach was used for the measurement of the τ polarisation in the decays $\tau \to \rho\nu$ where, in addition to $\cos\theta_h$, the angle ψ of the emission of the pions in the ρ rest frame was used to recuperate the spin information of the hadronic system. This angle is defined by:

$$\cos\psi = \frac{m_h}{\sqrt{m_h^2 - 4m_\pi^2}} \frac{E_{ch} - E_{neu}}{|\vec{p}_{ch} + \vec{p}_{neu}|}, \tag{10}$$

where $E_{ch}, \vec{p}_{ch}$ are the energy and momentum, in the laboratory frame, of the charged pion in the decay and $E_{neu}, \vec{p}_{neu}$ are the energy and momentum of the π^0.

In the inclusive one-prong hadronic analysis discussed in Section 7 the dominant decay channel is $\rho\nu$, but the polarisation extraction was performed including the other decay modes, in particular the $\tau \to a_1\nu$. In the one prong decay $\tau \to a_1\nu$, the a_1 decays to $\pi\pi^0\pi^0$ via the intermediate state $\rho\pi^0$. The variable $\cos\psi$ defined in Eq. 10 can also be defined experimentally for the $\tau \to a_1\nu \to \rho\pi^0\nu \to \pi\pi^0\pi^0\nu$ decay by summing over the two π^0's for the neutral energy E_{neu} and momentum $\vec{p}_{neu}$. The ρ carries the spin of the a_1 and although $\cos\psi$ no longer has the strict meaning of Eq. 10, it does retain sensitivity to the polarisation state of the a_1. The 2-dimensional distribution of $\cos\theta_h$ versus $\cos\psi$

for $\tau \to a_1\nu$ has a similar behaviour to that for $\tau \to \rho\nu$, but is somewhat more smeared. The $\tau \to a_1\nu$ and $\tau \to \rho\nu$ can thus be fitted simultaneously in an inclusive manner in terms of $\cos\theta_h$, $\cos\psi$ and hadronic invariant mass without significant loss of sensitivity by comparison with the $\tau \to \rho\nu$ channel alone [9]. On the other hand a significant increase in the statistics and reduction in the systematic errors is found due to the looser selection.

For the decay $\tau \to a_1\nu \to 3\pi^{\pm}\nu$ a method has been used which takes advantage of the most complete $\tau \to 3\pi^{\pm}\nu_\tau$ decay distribution determined in [10]. A fit to various moments of different angles in the 3π system is used. This is discussed in more detail in Section 6.5.

The selected τ decays in each analysis were grouped in six bins of equal width in $\cos\Theta$ between -0.73 and $+0.73$, plus two bins for the forward and backwards end caps up to ± 0.94. The polar angle of the decay products is a good approximation to the τ polar angle, the two angles being typically within 3° of each other.

The polarisation $\mathcal{P}_\tau$ in each $\cos\Theta$ bin for each analysis was estimated by fitting the data distributions to a linear sum of the predicted distributions for positive and negative polarisation states. These were generated by the KORALZ4.0 and TAUOLA2.5 programs [11] using Monte Carlo techniques, passed through a full detector simulation [12] and reconstructed with the same program as the data. A correction was made for the ratio of the acceptances of the different polarisation states. The simulated distributions used in the fits included background events. These were produced in the same way as for the signal events but using the following Monte Carlo event generators: DYMU3 [13] for $e^+e^- \to \mu^+\mu^-$ events; BABAMC [14], BHWIDE [15] and UNIBAB [16] for $e^+e^- \to e^+e^-$ events; JETSET 7.3 [17] for $e^+e^- \to q\bar{q}$ events; Berends-Daverveldt-Kleiss [18] for $e^+e^- \to (e^+e^-)e^+e^-$, $e^+e^- \to (e^+e^-)\mu^+\mu^-$ and $e^+e^- \to (e^+e^-)\tau^+\tau^-$ events.

3 The DELPHI detector

The DELPHI detector is described in detail elsewhere [19,12]. The sub-detector units particularly relevant for this analysis are summarised here. All these covered the full solid angle of the analysis except where specified. In the DELPHI reference frame the z-axis is taken along the direction of the e^- beam. The angle Θ is the polar angle defined with respect to the z-axis and ϕ is the azimuthal angle about this axis. The reconstruction of a charged particle trajectory in the barrel region of DELPHI resulted from a combination of the measurements in:

- the Vertex Detector (VD), made of three layers of 24 cm long single-sided silicon microstrip modules, at radii of 6.3, 9.0 and 11.0 cm from the beam axis. The space point precision was typically 8 μm and the two-track resolution was 100 μm in rϕ. At the start of 1994 run, the inner and outermost layers were equipped with double sided silicon detectors, giving an additional measurement in the z coordinate.
- the Inner Detector (ID), with an inner radius of 12 cm and an outer radius of 28 cm. A jet chamber measured 24 rϕ coordinates and provided track reconstruction. Its two-track resolution in rϕ was 1 mm and its spatial precision 50 μm. It was surrounded by an outer part which served mainly for triggering purposes.
- the Time Projection Chamber (TPC), extending from 30 to 122 cm in radius. This was the main detector for the track reconstruction. It provided up to 16 space points for pattern recognition and ionisation information extracted from 192 wires. Every 60° in ϕ there was a boundary region between read-out sectors about 1° wide which had no instrumentation. At $\cos\Theta = 0$ there was a cathode plane which caused a

reduced tracking efficiency in the polar angle range $|\cos\Theta| < 0.035$. The TPC had a two-track resolution of about 1.5 cm in rϕ and in z.

- the Outer Detector (OD) with 5 layers of drift cells at a radius of 2 metres from the beam axis. Each layer provided a space point with 110 μm precision in rϕ. It covered the barrel region in θ from 43° to 137°.

In the end caps, two chambers complemented the VD, ID and TPC

- the Forward Chamber A (FCA) mounted on each side of the TPC consisting of three modules of two staggered planes of drift tubes operated in limited streamer mode. It covered the polar angle range from 10° to 32°. The measured track elements had a precision of 290μm in x (horizontal), 240μm in y (vertical), 8.5 mrad in θ and 24 mrad in Φ.
- the Forward Chamber B (FCB), a drift chamber at $\pm$275 cm from the interaction point with 12 readout planes. It covered the polar angle range from 11° to 36°. The measured track elements had a precision of 150μm in x and y, 3.5 mrad in θ and $4/\sin(\theta)$ mrad in Φ.

In addition to the detectors mentioned above, the identification of the τ decay products relied on:

- the barrel electromagnetic calorimeter, a High density Projection Chamber (HPC), covering the polar angle region from 43° to 137°. This detector lay immediately outside the tracking detectors and inside the magnet coil. Eighteen radiation lengths deep for perpendicular incidence, its energy resolution was $\Delta E/E = 6.5\%$ for electrons with an energy of 45.6 GeV. It had a high granularity and provided nine layers of sampling of shower energies. It allowed a determination of the starting point of an electromagnetic shower with an accuracy of 3 mrads in polar angle and 0.006 radians in azimuthal angle. The HPC had a modularity of 15° in azimuthal angle. Between modules there was a region with a width of about 1° in azimuth where the resolution of electromagnetic showers was degraded. In this region a different treatment of the data had to be carried out for certain analyses.
- the forward electromagnetic calorimeter (FEMC), consisting of two arrays of 4532 Cherenkov lead glass blocks, starting at $\pm$284 cm from the interaction point. It covered the polar angle region from 8° to 35°. Its energy resolution was $\Delta E/E = 4.8\%$ for electrons with an energy of 45.6 GeV.
- the Hadron Calorimeter (HCAL), sensitive to hadronic showers and minimum ionising particles. It had a segmentation four layers deep, with a granularity of 3.75° in polar angle and 2.96° in azimuthal angle. Lying outside the magnet solenoid, it had a depth of 110 cm of iron.
- the barrel Muon Chambers (MUB) consisting of two layers of drift chambers, the first one situated after 90 cm of iron and the second outside the hadron calorimeter. The acceptance in polar angle of the outer layer was slightly smaller than the other barrel detectors and covered the range $|\cos\Theta| < 0.602$. The polar angle range $0.602 < |\cos\Theta|$ was covered by the forward Muon Chambers (MUF).

The Ring-Imaging Cherenkov detector (RICH), although not used in these analyses, had an important effect on the performance of the calorimetry as it contained the majority of the material in the DELPHI barrel region. Lying between the TPC and OD in radius, it covered the complete polar angle region of this analysis. it was 0.6 radiation lengths deep and 0.15 nuclear interaction lengths deep for particles of perpendicular incidence.

The DELPHI trigger was highly efficient for the τ final states, due to the redundancy existing between its different components. From the comparison of the response of

independent components, a trigger efficiency of $(99.98 \pm 0.01)\%$ within the geometrical acceptance of this analysis has been derived.

4 Particle identification and energy calibration

The detector response was studied extensively by using Monte Carlo simulations as well as various test samples of real data and simulation for which the particle identity was known with a high degree of certainty. Examples of such test samples are $e^+e^- \to e^+e^-(\gamma)$ events, $e^+e^- \to \mu^+\mu^-(\gamma)$ events, $e^+e^- \to (e^+e^-)e^+e^-$ events, $e^+e^- \to (e^+e^-)\mu^+\mu^-$ events and Compton events (scattering of a beam electron on a virtual photon). Test samples were also be produced using the redundancy of the detector for particle identification. An example of such a sample is $\tau \to \pi n\pi^0$ (n>0), selected using tagging of the π^0 from the electromagnetic calorimetry, which could be used to measure the response of the HCAL and muon chambers to charged pions. Further details regarding electron and muon identification variables can be found in [20].

4.1 TPC ionisation measurement

The energy loss, dE/dx, of charged particles through ionisation in the TPC, gives separation between electrons and more massive particles, particularly in the momentum range below 15 GeV/c. After the removal of 20% of wire hits with the largest pulse heights to remove tails due to delta rays, the resolution obtained on the dE/dx was 3% for isolated tracks in τ decays. The pull variable $\Pi^j_{dE/dx}$ for the hypothesis of particle type j (=e, π, μ,K) was defined as

$$\Pi^j_{dE/dx} = \frac{dE/dx|_{\rm meas} - dE/dx|_{\rm exp}(j)}{\sigma(dE/dx)}, \tag{11}$$

where $dE/dx|_{\rm meas}$ is the measured value, $dE/dx|_{exp}(j)$ is the expectation value for a particle of type j (dependent on its momentum) and $\sigma(dE/dx)$ is the resolution. Fig. 1a shows the spectra of $\Pi^e_{dE/dx}$, for a test sample of τ decays to electrons selected using the electromagnetic calorimeters. The separation between the means of the pion and electron signals is 3.5 standard deviations at a momentum of 5 GeV/c and 2.0 standard deviations at 15 GeV/c. Fig. 2a shows $\Pi^\pi_{dE/dx}$ for a hadron test sample, selected from τ decays.

4.2 Electromagnetic calorimetry

The HPC electromagnetic calorimeter is used for electron, photon and π^0 identification. For charged particles, E_{ass} is the energy of the electromagnetic shower in the HPC associated to the track. This association requires that the shower lie within about 4 cm of the track impact point on the HPC. For electrons E_{ass} should match the measured particle momentum within measurement errors. Muons, which are minimum ionising, deposit on average 200 MeV energy uniformly in depth in the HPC.

For hadrons the value is lower than for electrons because most hadrons pass through the HPC without interaction and those which do interact in the HPC leave a significant energy deposition only from the decays of π^0's in the interaction products. The ratio of the energy deposition in the HPC to the reconstructed momentum has a peak at one for electrons and a rising distribution towards zero for hadrons. The pull variable $\Pi_{E/p}$ is

defined as

$$\Pi_{E/p} = \frac{E_{ass}/p - 1}{\sigma\left(E_{ass}/p\right)}, \tag{12}$$

where $\sigma(E_{ass}/p)$ is the expected resolution for an electron of momentum p. $\Pi_{E/p}$ should thus be centred on zero with unit width for electrons and be negative for hadrons and muons. The distribution of $\Pi_{E/p}$ is plotted in Fig. 1b for a test sample of τ decays to electrons selected using the TPC ionisation, Hadron Calorimeter and Muon Chambers. There is a good separation for momenta larger than 1 GeV. Separation is best at highest momenta.

Electron rejection with high efficiency for hadron selection can be performed using the associated energy deposition in only the inner four layers of the HPC, corresponding to about six radiation lengths for perpendicular incidence, where electrons deposit a significant amount of energy, while hadrons have a small interacting probability. This is shown in Fig. 2b for hadrons from τ decays.

4.3 Photon and neutral pion identification

A photon pattern recognition [12] was performed which identified showers in the electromagnetic calorimeter and photons reconstructed from secondary interactions in the detector into five different classes:

- non interacting photons detected as showers in the electromagnetic calorimeter which are not associated to charged particles
- photons which converted in the material before the tracking devices and are therefore seen as pair of tracks
- photons which converted after the tracking devices and are therefore seen as pairs of neutral showers
- secondary photons from bremsstrahlung in the detector material
- showers initiated by a hadronic interaction in the HPC

Non-interacting photons were identified by electromagnetic showers in the HPC which were not associated to charged particles. K^0 hadronic interactions in the HPC may produce electromagnetic showers induced by a secondary π^0 that can be confused with a photon. Similarly, charged pion or kaons can produce secondary showers that are not associated to the charged particle and therefore considered as a photon. The high granularity of the HPC allowed many such showers to be rejected while retaining electromagnetic showers through the study of the longitudinal and transverse shower development. Further rejection of hadronic showers was performed by requiring the shower to have an energy greater than 0.5 GeV.

Converted photons in front of the tracking detectors are reconstructed using the TPC information. All pairs of candidate electron tracks are extrapolated backwards and a candidate conversion vertex is fitted. When a well reconstructed vertex is found close to a high density region of the detector, a photon is reconstructed from the two tracks. A second pass looks for single track candidates of asymmetric conversions or unresolved tracks from high energy photons, in a similar way.

If a conversion occurs in the outer wall of the TPC or in the RICH, the electron and positron are not reconstructed as tracks but are seen as two neutral showers in the HPC, increasing the neutral multiplicity. Most of these can be reconstructed using the track element of the OD, where the electron and positron are detected as charged particles,

together with the full three-dimensional position and direction information given by the HPC, which allows a vertex reconstruction as explained above.

When a photon is found close to a candidate electron track, its compatibility with a bremsstrahlung in a high density region of the detector was assessed, by checking if the photon direction was tangential to the electron trajectory.

In Fig. 3 the multiplicity and energy spectrum for the γ candidates for the τ inclusive sample is shown.

Due to the finite spatial resolution of the electromagnetic calorimeter, the probability for reconstructing a π^0 as either one or two neutral showers was a function of the energy of the π^0. This is illustrated in Fig. 4a which shows the fractions of simulated $\rho^{\pm}$ giving zero, one, two and more than two showers or reconstructed converted γ's in the HPC as functions of the generated π^0 energy. At energies below 2 GeV, π^0's appeared mostly as a single γ or remained undetected due to the energy threshold in the HPC. Above 10 GeV, the two photons tended to be close to one another and were often not resolved in the HPC as two showers, although a careful study of the shower profile can recognise a large fraction of these showers as formed from a π^0 as shown in Fig. 4b. In the intermediate energy range there is a mixture of all effects; in about one half of the cases the π^0 is resolved as two showers and in the other half only one shower is seen, either because the other γ has an energy below the HPC threshold or because the two photons are not resolved. These constraints apply only to photons which do not convert before the TPC. If at least one of the photons was reconstructed as a conversion before the TPC, the π^0 can give two photons even at higher energy. The small fraction of π^0's giving rise to more than two showers were due to unreconstructed photon conversions in front of the HPC, splitting of showers with large fluctuations and τ decays with a fake γ induced by hadronic interactions. The fraction of events without any γ corresponds to π^0's lost in boundary regions between modules of the HPC, failing the identification cuts or being wrongly associated to a track.

4.4 Hadron calorimetry and muon identification

A muon behaves as a minimum-ionising particle in the hadron calorimeter, penetrating through to the muon chambers. It tends to leave a constant amount of about 1.5 GeV in each of the four layers of the HCAL as well as several hits in the muon chambers associated to the track. On the contrary, charged hadrons either interact in the HPC or superconducting coil and do not leave any energy in the HCAL, or interact in the entry region of the HCAL depositing most of their energy in the two inner layers and very rarely reaching the muon chambers.

The different behaviour in the HCAL of hadrons and muons is reflected in several variables that can be used for hadron-muon separation. One of them is the mean energy deposition per hit layer of the hadron calorimeter E_{hlay}, defined by

$$E_{hlay} = E_{HCAL}/N_{Hlayers}, \tag{13}$$

where E_{HCAL} is the total energy associated to the charged particle in the HCAL and $N_{Hlayers}$ is the number of layers in the HCAL with deposited energy. In addition, the maximum energy deposited in any of the layers, or the energy deposited in the last layer, gives a significant separation, as does the number of hits in the muon chambers.

Some of these variables are shown in Fig. 5 for simulated and data muon test samples.

4.5 Momentum determination and scale

A good knowledge of the momentum and energy scales is crucial in the determination of the polarisation.

The precision on the momentum component transverse to the beam direction, p_t, obtained with the DELPHI tracking detectors was $\Delta(1/p_t) = 0.0008$ (GeV/c)$^{-1}$ for particles, other than electrons, with the beam momentum. An absolute calibration of the momentum was obtained from $e^+e^- \to \mu^+\mu^-$ events. For lower momenta, more representative of τ decays, the reconstructed momentum was checked from the reconstruction of the masses of the K^0_S and the J/ψ. The absolute momentum scale for particles other than electrons was estimated to be calibrated to a precision of 0.2% over the full momentum range.

4.6 Electromagnetic energy scale

The energy scale for electromagnetic showers in the HPC was estimated using electrons from $e^+e^- \to e^+e^-(\gamma)$ and Compton interactions as well as photons from final state radiative $e^+e^- \to e^+e^-\gamma$, $e^+e^- \to \mu^+\mu^-\gamma$ events and $\pi^0 \to \gamma\gamma$ from tau decays. These photons or electrons covered the full energy range 0.5 GeV to 40 GeV. A precision on the electromagnetic energy scale of 0.2% over the full energy range was estimated.

4.7 Electron momentum estimation

For the estimation of the momentum of electrons two variables were used. Firstly, for identification purposes, where an estimator from the tracking system was needed, use was made of the reconstructed momentum in the tracking detectors. Secondly, for the extraction of the τ polarisation from the sample of identified electron candidates, use was made of an estimator based on the combined information from the tracking system and the electromagnetic calorimetry to estimate as accurately as possible the true momentum of the decay electrons. The combination was based on the observation that both the measured momentum, p, and the associated electromagnetic energy, E_{ass}, tended to be biased towards lower values than the true electron momentum. Whereas the momentum bias originated from bremsstrahlung in front of the TPC, the bias on the electromagnetic energy was primarily caused by edge effects in the HPC close to boundary regions between modules. The value of E_{ass}/p was used to indicate whether p or E_{ass} was a more reliable estimator for a given electron candidate. This relied on the fact that the downward biases of the two estimators cause opposite effects on the value of E_{ass}/p. An algorithm was constructed such that, when E_{ass}/p was consistent with the electron hypothesis, i.e. close to unity, the two estimators p and E_{ass} were combined through a weighted mean, where the weights were inversely proportional to the square of the measurement uncertainties. However, the further the value of E_{ass}/p was away from the electron hypothesis, the more the weight of the estimator with the lower value was scaled down relative to the other. In this way the downward bias in the momentum estimation was reduced significantly and the precision was improved by exploiting all available information. The final electron momentum estimator, p_{el}, was then obtained by adding to this weighted mean the energy of any γ's tagged as originating from a bremsstrahlung.

The calibration of p_{el} was performed with electron samples where the true momentum was known from kinematic constraints. Non-radiative decays of the Z into e^+e^- pairs provided a high statistics calibration of the high end of the momentum spectrum. Ra-

diative $e^+e^- \to e^+e^-\gamma$ events covered the important momentum range between 20 and 35 GeV/c.

From a comparison of the real data and simulation for the three test samples, p_{el} was shown to be calibrated to a precision of 0.5%, arising from the limited number of events in the test sample. Note that although the scale of this estimator is less precisely known than both the momentum and the electromagnetic energy (due to the fact that fewer events could be used in the test sample), the general behaviour of the estimator was much better and leads to smaller systematic errors. Simulation studies showed that for a given true value of momentum: the distribution of the estimator p_{el} was better fit by a Gaussian function than either the momentum or the associated electromagnetic energy; the width of the Gaussian was narrower; and the tails (due to radiation) were reduced.

5 Event sample

The data sample corresponded to an integrated luminosity of 109.8 pb^{-1} composed of: 47.4 pb^{-1} at E_{cm} = 91.2 GeV in 1994; 29.6 pb^{-1} at three centre-of-mass energies around the Z peak for 1993 (9.4 pb^{-1} at 89.2 GeV, 15.7pb^{-1} at 91.2 GeV and 4.5 pb^{-1} at 93.2 GeV); 32.8 pb^{-1} at similar centre-of-mass energies around the Z peak for 1995 (9.2 pb^{-1} at 89.2 GeV, 14.3pb^{-1} at 91.2 GeV and 9.3 pb^{-1} at 93.2 GeV). The previously published data [5] corresponded to 33.6 pb^{-1} with data taken from E_{cm} = 88.5 to 93.7 GeV in 1990, 1991 and 1992. The data sample was selected according to the criteria outlined below. It consisted of a high purity sample of dileptonic events ($e^+e^- \to e^+e^-$, $\mu^+\mu^-$, $\tau^+\tau^-$) where cosmic rays, $e^+e^- \to q\bar{q}$ and $e^+e^- \to (e^+e^-)X$ two-photon events had been removed. Backgrounds from the e^+e^- and $\mu^+\mu^-$ final states were removed later in a channel specific way in order to minimise biases.

At LEP energies, a $\tau^+\tau^-$ event appears as two highly collimated low multiplicity jets in approximately opposite directions. An event was separated into hemispheres by a plane perpendicular to the event thrust axis, where the thrust was calculated using all charged particles. To be included in the sample, it was required that the highest momentum charged particle in at least one of the two hemispheres lie in the polar angle region $|\cos\Theta| < 0.940$.

Background from $e^+e^- \to q\bar{q}$ events was reduced by requiring a charged particle multiplicity less than or equal to six, and an isolation angle, defined as the minimum angle between any two charged particles in different hemispheres, greater than 160°.

Cosmic rays and beam-gas events were rejected by requiring that the highest momentum charged particle in each hemisphere be consistent with coming from the interaction region. The points of closest approach were both required to be less than 4.5 cm in z and less than 1.5 cm in the rϕ plane, with at least one of them being less than 0.3 cm in the rϕ plane. It was furthermore required that these particles have a difference in z of their points of closest approach at the interaction region of less than 3 cm. The offset in z of tracks in opposite hemispheres of the TPC was sensitive to the time of passage of a cosmic ray event with respect to the interaction time of the beams. The background left in the selected sample was computed from the data by interpolating the distributions outside the selected regions.

Two-photon events were removed by requiring total energy in the event to be greater than 8 GeV and total transverse momentum to be greater than 0.4 GeV/c.

The preceding requirements were used to produce a sample which contained most of the $\tau^+\tau^-$ events as well as a large fraction of e^+e^- and $\mu^+\mu^-$ events, while other backgrounds were suppressed. It was estimated from simulation to have an efficiency of 87% for $\tau^+\tau^-$

within the polar angle fiducial region. Approximately 105000 $\tau^+\tau^-$ events remained after application of all the cuts described above (including the whole statistics from 1990 to 1995). Real data and simulated test samples were used to estimate the background in the sample: 0.8% of selected events were estimated to come from $e^+e^- \to q\bar{q}$ events and 0.4% from two-photon events. The cosmic ray contamination was negligible.

Contamination from $e^+e^- \to \mu^+\mu^-$ and $e^+e^- \to e^+e^-$ events in the samples where both taus had decayed to a single track was reduced by requiring that the event acollinearity $\theta_{acol} = \cos^{-1}(-\vec{p}_1 \cdot \vec{p}_2/(|\vec{p}_1||\vec{p}_2|))$ be greater than 0.5°. The variables $\vec{p}_1$ and $\vec{p}_2$ are the momenta of the highest momentum charged particles in either hemisphere 1 or 2. This cut was applied for all except the $\tau \to \pi(\mathrm{K})\nu$ analysis where the $\mu^+\mu^-$ and e^+e^- final states were not significant backgrounds.

For the analyses of $e\nu\bar{\nu}$, $\mu\nu\bar{\nu}$, $\rho\nu$ and $a_1\nu$ decays, the background from $\mu^+\mu^-$ and e^+e^- final states was reduced further by requiring that $p_{rad} = (|\vec{p}_1|^2 + |\vec{p}_2|^2)^{1/2}$ be less than the beam momentum p_{beam} and that $E_{rad} = (E_1^2 + E_2^2)^{1/2}$ be less than the beam energy E_{beam}. The variables E_1 and E_2 are the total electromagnetic energies deposited in cones of half angle 30° about the momentum vectors $\vec{p}_1$ and $\vec{p}_2$ respectively.

Different dilepton rejection cuts were used in the neural network analysis. In addition to the acollinearity cut, events with a one versus one charged particle topology were rejected with cuts depending on the value of the variable PE_{max}. This was defined as the maximum of $|\vec{p}_1|$, $|\vec{p}_2|$, $E_{ass,1}$ and $E_{ass,2}$, where $E_{ass,i}$ was the electromagnetic energy associated to the highest momentum particle in hemisphere i. Bhabha background was reduced by removing events with PE_{max} greater than $0.8 \times E_{beam}$ and $E_{ass}/|\vec{p}|$ greater than 0.5 for the hemisphere from which PE_{max} was obtained. Furthermore, Bhabha events with potentially poorly measured electromagnetic energy were rejected if $PE_{max} > 0.8 \times E_{beam}$ and the extrapolation of the charged particle track to the HPC lay within 1° of the centre of an HPC azimuthal boundary. Dimuon background was reduced by rejecting events with PE_{max} greater than $0.88 \times E_{beam}$ and $E_{ass}/|\vec{p}|$ less than 0.06 for the hemisphere from which PE_{max} was obtained, consistent with the signal of a minimum ionising particle in the HPC.

6 Exclusive τ decays

6.1 $\tau \to e\nu\bar{\nu}$

A $\tau \to e\nu\bar{\nu}$ decay has the signature of an isolated charged particle which produces an electromagnetic shower in the HPC and leaves an ionisation deposition in the TPC corresponding to the plateau region above the relativistic rise. Backgrounds from other τ decays arise principally from one-prong hadronic decays where either the hadron interacts early in the HPC or an accompanying π^0 decay is wrongly associated to the charged particle track. The polarisation was derived from a fit to the spectrum of the electron momentum estimator p_{el} described in Section 4.7.

To be identified as an electron candidate [20] it was required that the hemisphere contain a single charged particle whose momentum was greater than $0.01 \times p_{beam}$. To ensure optimal performance of the HPC, it was required that the track lie in the polar angle region $0.035 < |\cos\Theta| < 0.707$, and its extrapolation to the HPC be further than 1° from the centre of an HPC azimuthal boundary region.

As dE/dx played an important role in the selection, it was demanded that the particle track had at least 38 wires with an ionisation measurement in the TPC. This led to a 4% loss of tracks around the boundary regions of the TPC sectors which was well described

by the simulation. It was required that the dE/dx measurement be compatible with that of an electron by demanding that the pull $\Pi^{e}_{dE/dx}$ be greater than -2. This significantly reduced the background from hadrons and muons, especially at low momentum, with a very low loss of signal.

The background was reduced further with a logical OR of two independent sets of selection criteria based on the HPC and the TPC dE/dx respectively. This ensured a high identification efficiency over the full momentum range. It was required that:

- either the associated HPC energy was compatible with the momentum p, the pull $\Pi_{E/p}$ was greater than -1.5 and the momentum was greater than $0.05 \times p_{beam}$
- or the TPC dE/dx signal more than three standard deviations above that expected for a pion, $\Pi^{\pi}_{dE/dx} > 3$, and the momentum was less than $0.5 \times p_{beam}$.

The first criterion had an overall efficiency of 88%. The second criterion had an overall efficiency of 36%, varying from 99.5% for the lowest momentum particles to 10% for momenta of about 20 GeV/c

In order to reduce the residual background from hadronic τ decays it was required that the particle had no muon chamber hits and no associated energy in the HCAL beyond the first layer. Furthermore there could be no neutral HPC shower with an energy greater than 4 GeV in a cone of half angle 18° about the track. Neutral showers compatible with a bremsstrahlung photon were not included in this cut.

The identification criteria were studied using test samples of real data. The efficiency in the high momentum region was obtained from a sample of $e^+e^- \to e^+e^-$ events and in the low momentum region from a sample of $e^+e^- \to (e^+e^-)e^+e^-$ events. For intermediate momenta the redundancy between the dE/dx and HPC criteria was exploited to give a precise determination of each of the two. Since the simulation showed that the two criteria were instrumentally uncorrelated, the overall efficiency was computed from the two independent measurements. An identification efficiency of 90% within the angular and momentum acceptance (excluding the loss due to the cut on the number of TPC wires for dE/dx) was derived. In a similar manner, using the redundancy of the dE/dx and HPC identification requirements, the background from other τ decays, primarily the $\tau \to \rho\nu$ channel, was found to be $(2.2 \pm 0.2)\%$

Most $e^+e^- \to e^+e^-$ events were rejected with the event acollinearity cut $\theta_{acol} > 0.5°$. Remaining Bhabha contamination was reduced with the cuts on P_{rad} and E_{rad} defined in Section 5

Background from $e^+e^- \to (e^+e^-)e^+e^-$ events was reduced in events with only one charged particle in each hemisphere, where both had a momentum less than $0.2 \times p_{beam}$, by requiring that the dE/dx for the opposite hemisphere track be inconsistent with that of an electron.

The selection efficiency within the angular acceptance for $\tau \to e\nu\bar{\nu}$ decays was 72% after the Bhabha rejection cuts, with a background of $(1.6 \pm 0.5)\%$ from Bhabha events and $(0.33 \pm 0.10)\%$ from $e^+e^- \to (e^+e^-)e^+e^-$ events. The background from other τ decays was $(2.1 \pm 0.2)\%$. The selected sample consisted of 18273 candidate decays. The p_{el} spectrum summed over all bins in $\cos\Theta$ is shown in Fig. 6, with the simulated spectrum for the fitted value of $\langle \mathcal{P}_\tau \rangle$ superimposed.

The polarisation $\mathcal{P}_\tau$ was fitted in each of the six bins of $\cos\Theta$ as described in Section 2. The results are shown in Table 1. The extraction of the electroweak parameters from these numbers is described in Section 9.2 and results are given in Table 9

The contributions to the systematic error in $\langle \mathcal{P}_\tau \rangle$ (summarised in Table 3) included that due to the identification efficiency (0.025), estimated from cross-checking of dE/dx and

HPC cuts. The uncertainty from backgrounds had two contributions, one corresponding to the uncertainty of their amount, which contributed with 0.020, and another for the momentum description of the Bhabha background, mainly due to the treatment of the double radiation in the Monte Carlo generators [14–16], contributing with 0.015. The uncertainty in the electron momentum scale gave an uncertainty of 0.030 and the finite simulation statistics an error of 0.013, resulting in a total systematic uncertainty of 0.048.

	91–92	93–95	91–95
cosΘ range	$\tau \to e\nu\bar{\nu}$		
−0.732,−0.488	-0.063 ± 0.171	-0.082 ± 0.103	-0.078 ± 0.088
−0.488,−0.244	-0.118 ± 0.169	$+0.057 \pm 0.100$	$+0.070 \pm 0.086$
−0.244, 0.000	$+0.044 \pm 0.217$	-0.165 ± 0.106	-0.132 ± 0.096
0.000,+0.244	-0.583 ± 0.226	-0.278 ± 0.106	-0.323 ± 0.096
+0.244,+0.488	-0.180 ± 0.174	-0.238 ± 0.101	-0.226 ± 0.087
+0.488,+0.732	-0.315 ± 0.173	-0.298 ± 0.107	-0.302 ± 0.091
cosΘ range	$\tau \to \mu\nu\bar{\nu}$		
−0.940,−0.732	−	-0.018 ± 0.088	-0.018 ± 0.088
−0.732,−0.488	-0.166 ± 0.159	$+0.058 \pm 0.079$	$+0.022 \pm 0.071$
−0.488,−0.244	-0.040 ± 0.166	-0.147 ± 0.086	-0.129 ± 0.076
−0.244, 0.000	$+0.109 \pm 0.182$	-0.047 ± 0.096	-0.019 ± 0.085
0.000,+0.244	$+0.219 \pm 0.181$	-0.118 ± 0.099	-0.054 ± 0.087
+0.244,+0.488	-0.275 ± 0.175	-0.295 ± 0.088	-0.292 ± 0.079
+0.488,+0.732	$+0.009 \pm 0.146$	-0.233 ± 0.083	-0.185 ± 0.072
+0.732,+0.940	−	-0.115 ± 0.088	-0.115 ± 0.088
cosΘ range	$\tau \to \pi\nu$		
−0.732,−0.488	-0.191 ± 0.091	-0.102 ± 0.060	-0.124 ± 0.050
−0.488,−0.244	-0.104 ± 0.084	-0.048 ± 0.054	-0.061 ± 0.045
−0.244, 0.000	-0.008 ± 0.095	-0.282 ± 0.060	-0.220 ± 0.051
0.000,+0.244	-0.281 ± 0.093	-0.026 ± 0.059	-0.084 ± 0.050
+0.244,+0.488	-0.295 ± 0.082	-0.300 ± 0.050	-0.399 ± 0.043
+0.488,+0.732	-0.295 ± 0.087	-0.315 ± 0.059	-0.310 ± 0.049
cosΘ range	$\tau \to \rho\nu$		
−0.732,−0.488	-0.099 ± 0.079	$+0.072 \pm 0.051$	$+0.031 \pm 0.043$
−0.488,−0.244	-0.037 ± 0.081	-0.094 ± 0.053	-0.080 ± 0.045
−0.244, 0.000	$+0.080 \pm 0.079$	-0.152 ± 0.062	-0.079 ± 0.049
0.000,+0.244	$+0.123 \pm 0.077$	-0.126 ± 0.061	-0.047 ± 0.048
+0.244,+0.488	-0.349 ± 0.083	-0.207 ± 0.053	-0.240 ± 0.044
+0.488,+0.732	-0.141 ± 0.079	-0.273 ± 0.048	-0.244 ± 0.041

Table 1: τ polarisation values in bins of cosΘ for the $e\nu\bar{\nu}$, $\mu\nu\bar{\nu}$, $\pi\nu$, and $\rho\nu$ analyses, for the 1991 and 1992 published data, 1993 to 1995 new data and combination of 1991 to 1995. Errors are statistical only.

	91–92	93–95	91–95
cosΘ range	$\tau \to a_1\nu$		
−0.732,−0.488	$+0.137 \pm 0.141$	-0.045 ± 084	-0.006 ± 0.072
−0.488,−0.244	-0.110 ± 0.145	$+0.056 \pm 0.091$	$+0.017 \pm 0.077$
−0.244, 0.000	-0.136 ± 0.141	-0.108 ± 0.112	-0.117 ± 0.088
0.000,+0.244	-0.100 ± 0.202	-0.240 ± 0.107	-0.215 ± 0.094
+0.244,+0.488	-0.420 ± 0.162	-0.138 ± 0.098	-0.199 ± 0.084
+0.488,+0.732	-0.363 ± 0.177	-0.247 ± 0.087	-0.265 ± 0.078
cosΘ range	Inclusive		
−0.940,−0.732	−	$+0.006 \pm 0.046$	$+0.006 \pm 0.046$
−0.732,−0.488	-0.115 ± 0.051	-0.002 ± 0.025	-0.019 ± 0.022
−0.488,−0.244	$+0.061 \pm 0.055$	-0.014 ± 0.026	-0.004 ± 0.023
−0.244, 0.000	-0.105 ± 0.055	-0.116 ± 0.028	-0.114 ± 0.025
0.000,+0.244	-0.165 ± 0.057	-0.137 ± 0.028	-0.141 ± 0.025
+0.244,+0.488	-0.268 ± 0.048	-0.189 ± 0.025	-0.203 ± 0.022
+0.488,+0.732	-0.273 ± 0.045	-0.256 ± 0.024	-0.259 ± 0.021
+0.732,+0.940	−	-0.209 ± 0.045	-0.209 ± 0.045
cosΘ range	Neural network		
−0.732,−0.488	−	-0.018 ± 0.028	-0.018 ± 0.028
−0.488,−0.244	−	-0.046 ± 0.029	-0.046 ± 0.029
−0.244, 0.000	−	-0.080 ± 0.034	-0.080 ± 0.034
0.000,+0.244	−	-0.181 ± 0.034	-0.181 ± 0.034
+0.244,+0.488	−	-0.225 ± 0.028	-0.225 ± 0.028
+0.488,+0.732	−	-0.237 ± 0.027	-0.237 ± 0.027

Table 2: τ polarisation values in bins of cosΘ for the $a_1\nu$, inclusive and neural network analyses, for the 1991 and 1992 published data, 1993 to 1995 new data and combination of 1991 to 1995. Errors are statistical only.

6.2 $\tau \to \mu\nu\bar{\nu}$

In $\tau \to \mu\nu\bar{\nu}$ decays the τ polarisation was measured using the reconstructed momentum spectrum for the candidate decays, which were identified using techniques described in Section 4.4.

In order to identify such a decay it was required [20] that there be only one charged particle track in a hemisphere and that it be able to penetrate to the outside of the DELPHI magnet iron. Thus the charged particle reconstructed momentum had to be greater than $0.05 \times p_{beam}$. To maintain a high efficiency and good purity over all the polar angle range a particle was identified as a muon if one of the two following criteria was fulfilled:

- no single HCAL layer had more than 3 GeV of deposited energy and the outermost had at least 0.2 GeV
- at least two hits in the muon chambers were associated to the track

Since the two cuts are independent except for very low momentum muons that stop in the iron, the efficiency of each one can be estimated from the data itself. The comparison of the efficiency and its momentum dependence estimated from data and simulation provided a powerful cross-check of this stage of the selection.

Most of the remaining background came from energetic charged pions reaching the outer HCAL layers or even the muon chambers. Those hemispheres were removed requiring the average HCAL energy (defined in Section 4.4) to be less than 2 GeV. Since a large fraction of the τ decays to charged pions also involve π^0's, this background was suppressed further by requiring that at most 3 GeV was detected in the electromagnetic calorimeters in a cone of 18° degrees around the track.

After these cuts, the fraction of remaining pions tracks was small but there was still an important contribution from muons not produced in a τ decay but from the reaction $e^+e^- \to \mu^+\mu^-$. Additional requirements were applied to reject these. Events with $P_{rad} > 1$ (as defined in Section 5) or a momentum larger than 80% of E_{beam} in the hemisphere opposite to the muon candidate were discarded. When both τ's in the event were identified as decaying to muons, only those with a total energy less than 70% of the E_{cm} were accepted.

The detection efficiency and its momentum dependence were estimated from simulation and were checked and corrected using the redundancy of the HCAL and MUB as well as with μ test samples [20]. The misidentification efficiency of the HCAL and MUB criteria for background τ decays was checked by a comparison of real data and simulated samples of $\tau \to h\nu n\pi^0$, (n>0), selected by the existence of one or more tagged π^0's.

In the barrel the number of candidate τ decays remaining after these cuts was 20898. The overall efficiency to identify a $\tau \to \mu\nu\bar{\nu}$ decay inside the barrel angular and momentum acceptance was 85%. The background was composed of (1.39 ± 0.08)% from other τ decays, (0.42 ± 0.04)% from $\mu^+\mu^-$ events, (1.19 ± 0.08)% from $e^+e^- \to (e^+e^-)\mu^+\mu^-$ events, (0.40 ± 0.04)% from $e^+e^- \to (e^+e^-)\tau^+\tau^-$ events and (0.17 ± 0.01)% from cosmic rays.

In the end-caps, additional cuts were needed to reduce the higher background from two photon collisions. The acollinearity cut described in Section 5 was tightened to 1° and energy deposition in the luminosity monitors was required to be less than 5 GeV. A total of 6962 candidates were selected with an efficiency of 81% and a total background of 8.0% which was dominated by $e^+e^- \to (e^+e^-)\mu^+\mu^-$ (3.4%), $\mu^+\mu^-$ (1.4%) and other τ decays (2.6%).

The momentum spectrum summed over all bins in cosΘ is shown in Fig. 7, with the simulated spectrum for the fitted value of $\langle \mathcal{P}_\tau \rangle$ superimposed.

The polarisation $\mathcal{P}_\tau$ was fitted in each of the eight bins of cosΘ as described in Section 2. The results are shown in Table 1. The extraction of the electroweak parameters from these numbers is described in Section 9.2 and results are given in Table 9

The effect on $\langle \mathcal{P}_\tau \rangle$ of the uncertainties on the estimation of the efficiency and misidentification probability of hadronic τ decays amounted to 0.005 and 0.001 respectively in the barrel. Other significant contributions to the systematic errors were: contamination from $e^+e^- \to \mu^+\mu^-$ events (0.007), contamination from two photon events (0.003); the momentum resolution uncertainty and momentum scale (0.009); the finite simulation statistics (0.009). The effect of other backgrounds was negligible. The total systematic uncertainty was 0.018 and the main contributions are summarised in Table 3.

Systematic errors in the end cap were treated in a similar way. The total uncertainty was 0.033 and included the following main contributions: the uncertainty in the muon identification momentum dependence (0.010); the uncertainty in the background contamination from hadronic misidentification (0.001); contamination from $e^+e^- \to \mu^+\mu^-$ events (0.018), $e^+e^- \to (e^+e^-)\mu^+\mu^-$ and $e^+e^- \to (e^+e^-)\tau^+\tau^-$ events (0.008); the momentum resolution uncertainty and momentum scale (0.016) and the finite simulation statistics (0.016). The effect of other backgrounds was negligible.

6.3 $\tau \to \pi\nu$

A typical $\pi\nu$ or Kν decay is characterised by a single isolated charged particle which deposits energy deep in the HPC or in the HCAL. The separation of pions from electrons and muons requires the use of almost all components of the DELPHI detector. An important background arises from $\tau \to \rho\nu \to \pi\pi^0\nu$ decays where the π^0 is not detected due to threshold effects, dead regions in the calorimeter or photons failing the quality cuts.

For efficient suppression of muons it was required that the isolated charged particle has a momentum exceeding $0.067 \times p_{beam}$. To avoid inefficient regions of the calorimetry it was also required to lie in the polar angular region $0.035 < |\cos\Theta| < 0.707$.

The separation of pions from muons relied on the observed signal in the HCAL and muon chambers as described in Section 4.4. Pion behaviour in the calorimeters can be divided into three categories: pions which interact in the HPC; pions which stop early in the HCAL; and pions which 'punch through' to the outer part of the HCAL and muon chambers. For a better treatment of each case, the candidates were treated differently according to the mean energy per layer deposited in the HCAL as defined in Section 4.4. In the range $0 < E_{hlay} < 3$ GeV the ratio of pions to muons was low. As these pions tended to have low momentum and did not penetrate deep into the HCAL, a muon veto was applied by excluding all particles which were observed in the muon chambers or the outer layer of the HCAL. For $E_{hlay} \geq 3$ GeV the ratio of pions to muons was high and a muon veto was applied by excluding particles only if they were observed in the outer layers of the muon chambers. Finally if no energy deposition was observed, the pion tended to have interacted in the HPC and only hemispheres with at least 0.5 GeV electromagnetic deposition and no muon chamber hits were retained.

For electron rejection it was required that the electromagnetic energy deposited by the charged particle in the first four HPC layers did not exceed 350 MeV, and that the dE/dx did not exceed the expected signal of a pion by more than two standard deviations: $\Pi^{\pi}_{dE/dx} < 2$. Within 0.5° of an azimuthal boundary between HPC modules, where the

rejection power of the HPC criterion was poorer, the dE/dx requirement was tightened by requiring that $\Pi^{\pi}_{dE/dx} < 1$.

A further reduction of the background from electrons and muons was ensured by requiring that the charged particle was either observed in the HCAL or deposited at least 500 MeV in the last five layers of the HPC.

The remaining internal background, from other τ decays, was dominated by hadronic τ decays containing π^0's. Those were rejected with the requirement that there be no identified photons in a cone of half angle 18° around the charged pion.

The background from $e^+e^- \to e^+e^-(\gamma)$ was reduced with the E_{rad} cut described in Section 5 and $e^+e^- \to \mu^+\mu^-(\gamma)$ events were rejected by requirements on the hemisphere opposite to the identified candidate decay in order not to bias the pion momentum spectrum. It was required that the highest momentum charged particle in that hemisphere lie in the polar angle region $0.035 < |\cos\Theta| < 0.732$ and that its momentum was less than $0.75 \times p_{beam}$.

The identification efficiency and misidentification probabilities were estimated from simulation and checked using test samples, applying small corrections where needed. The efficiencies of the muon and electron rejection criteria were investigated using a sample of charged hadrons from τ decays to $\rho\nu$ and $a_1\nu$ tagged by the presence of a π^0 in the HPC. The misidentification probabilities were obtained from samples of electrons and muons tagged by kinematic constraints or by the use of independent detector components.

The overall identification efficiency within the angular and momentum acceptance was estimated to be 58%.

A total of 6402 candidate decays was selected. The estimated background from other τ decays was 9.9%, with a contribution of 5.3% from the $\rho\nu$ mode. The background of Z decays into electron or muon pairs was 0.6%. Other backgrounds were negligible.

The polarisation $\mathcal{P}_\tau$ was fitted in each of the six bins of $\cos\Theta$ as described in Section 2. The results are shown in Table 1. The extraction of the electroweak parameters from these numbers is described in Section 9.2 and results are given in Table 9

The momentum spectrum of all selected candidates is shown in Fig. 8 with the simulated spectrum for the fitted value of $\langle\mathcal{P}_\tau\rangle$ superimposed.

The uncertainty in $\langle\mathcal{P}_\tau\rangle$ due to the momentum scale was negligible for this channel. The systematic uncertainty in $\langle\mathcal{P}_\tau\rangle$ was 0.022 and included the following contributions (summarised in Table 3): the muon rejection efficiency (0.017); electron rejection efficiency (0.007); γ rejection efficiency (0.010); and external background estimates (0.002) which were dominated by the $\mu^+\mu^-$ and e^+e^- background. The uncertainty due to radiative corrections to the τ decay process [21] contributed an error of 0.001. The uncertainty due to the finite simulation statistics was 0.007.

6.4 $\tau \to \rho\nu$

The τ decay to $\rho\nu$ was selected by requesting an isolated charged particle in the polar angle region $|\cos\Theta| < 0.732$ with an accompanying π^0 candidate also in the barrel and within 20° of the charged particle.

On account of the different detector responses as a function of π^0 energy (Section 4.3) a candidate ρ had to have one of the two following topologies:

- two photons with an angle between them of less than 10° and an invariant mass lying in the range 0.04 GeV/c^2 to 0.25 GeV/c^2;
- a single shower with more than 6 GeV and with a shape compatible with that of a π^0.

The $\gamma\gamma$ invariant mass for all the candidate hemispheres in the two photons topologies and the $\pi\pi^0$ invariant mass distributions are shown in Fig. 9. To reduce background it was required that the reconstructed total invariant mass lie in the range 0.48 GeV/c^2 to 1.20 GeV/c^2. The sample remaining after the cuts contained 19734 τ decays. The selection efficiency inside the angular acceptance was 45%. The remaining background from other τ decays was 17.4% dominated by a contribution of 14.7% from the $\pi\pi^0\pi^0\nu$ channel; Contamination from $e^+e^- \to e^+e^-(\gamma)$ and $e^+e^- \to \mu^+\mu^-(\gamma)$ events was negligible.

The polarisation was estimated using the variable ξ described in Eq. 9. This variable was a function of the decay angle of the ρ in the τ rest frame, of the $\pi^\pm$ in the ρ rest frame and of the hadronic invariant mass.

The polarisation $\mathcal{P}_\tau$ was fitted in each of the six bins of cosΘ as described in Section 2. The results are shown in Table 1. The extraction of the electroweak parameters from these numbers is described in Section 9.2 and results are given in Table 9

The ξ spectrum summed over all bins in cosΘ is shown in Fig. 10, with the simulated spectrum for the fitted value of $\langle\mathcal{P}_\tau\rangle$ superimposed.

The systematic uncertainty in $\langle\mathcal{P}_\tau\rangle$ due to the finite statistics of the simulation was 0.006. An uncertainty of 0.009 due to the π^0's identification was estimated by varying the identification criteria and from data and simulation comparison. Uncertainty of the HPC energy resolution and scale resulted in an error of 0.011. The uncertainty coming from the internal background was 0.008 and was dominated by the estimation of the fraction of a_1 being accepted by the total invariant mass cut. By following the same procedure as in Section 6.3 the uncertainty due to radiative corrections was estimated to be 0.001. The uncertainty in the momentum scale had a negligible effect. The total systematic uncertainty was 0.017 and the main contributions are summarised in Table 3.

6.5 $\tau \to a_1\nu \to \pi^-\pi^+\pi^\pm\nu$

The decay $\tau \to 3\pi^\pm\nu_\tau$ is characterised by a topology containing three charged particles with no neutral electromagnetic energy present in that hemisphere.

The first requirement in the selection of such events was that the hemisphere contain three charged particles with the absolute value of the sum of their charges equal to unity. The vector sum of their momenta, $\vec{P}^{3\pi}_{vis}$, had to lie in the polar angle region $|\cos\Theta| < 0.732$ and have a magnitude greater than $\frac{1}{3}\,E_{beam}$. As the three particles should originate from a τ decay it was required that the invariant mass of the 3π system be less than 2 GeV/c^2.

To reduce background from one-prong τ decays with accompanying photons which converted and were not identified, the microvertex detector was used. Most conversions take place after this detector which, together with the beam-pipe, accounts for about 2% of a radiation length of material. Most e^+e^- from conversions are thus not expected to produce a signal in the microvertex detector. It was demanded that at least two of the three tracks have at least two associated hits in the microvertex detector.

Hemispheres with three prongs accompanied by photons were rejected except in the case of a single photon with less than 1.5 GeV. These photons had to satisfy the requirements described in Section 4.3. A photon was assigned to the 3π hemisphere if the angle between the photon and the 3π resultant momentum direction was less than 30°.

A $\tau \to 3\pi n\gamma\nu$ (n>0) decay can also fake a $\tau \to 3\pi^\pm\nu_\tau$ event if the photons overlap with the charged particles and are associated to them. To reject these decays and suppress photon conversions further, an additional cut was applied, $E_4^{3\pi}/P_{vis}^{3\pi} < 0.3$, where $E_4^{3\pi}$ is the sum of the energy deposited in the first four layers of the HPC and associated to the tracks.

To reduce non-resonant background, it was required that at least one of the two possible $\pi^+\pi^-$ combinations have an invariant mass in the range 0.6 GeV/c^2 $< m_{\pi^+\pi^-} <$ 1.2 GeV/c^2. This cut was asymmetric with respect to the ρ peak because the background should peak in the low mass region, as was the case for the distribution of like sign charged combinations.

These cuts produced a sample of 6827 candidate $a_1\nu$. The efficiency within the polar angle acceptance was 47%. The background from other τ decays was estimated to be 14.1%, while other backgrounds were negligible. The 3π invariant mass distribution is shown in Fig. 11.

The $\mathcal{P}_\tau$ measurement was performed with a method proposed in [8] based on moments of various decay distributions, as advocated by Kühn and Mirkes [10], whose notation is followed below.

The $\tau \to 3\pi^\pm\nu_\tau$ decay rate can be written as

$$d\Gamma_{\tau\to\pi\pi\pi\nu_\tau} \propto \sum_X \bar{L}_X W_X d\gamma d\cos\theta_h d\cos\beta dQ^2 ds_1 ds_2, \tag{14}$$

where θ_h is the angle in the τ rest frame between the τ flight direction and the direction of emission of the hadronic system, β is the angle in the hadronic rest frame between the normal to the 3π decay plane and the direction of the hadrons in the laboratory system, and γ corresponds to a rotation around the normal to the decay plane and determines the orientation of the pions within their production plane. The hadronic structure functions W_X contain the dynamics of the 3π decay and depend in general on the invariant masses s_1, s_2 of the two $\pi^+\pi^-$ combinations and on Q^2, the invariant mass of the 3π system. The lepton factors $\bar{L}_X$ are functions of the angles θ_h, β and γ. They also depend on $\mathcal{P}_\tau$.

The hadronic structure functions W_X do not factorize in expression (14). Hence, for a given set of $\cos\theta_h$, γ, $\cos\beta$, s_1, s_2, and Q^2, the $W_X(s_1, s_2, Q^2)$ must be calculated in order to perform a fit to the polarisation. In general, the result will depend on the particular model assumed for the hadronic current.

The values of $\mathcal{P}_\tau$ are derived from a combined fit to the $\cos\theta_h$ distribution and the one-dimensional distributions of the following set of moments as a function of $\cos\theta_h$:

$$\langle(3\cos^2\beta - 1)/2\rangle, \quad \langle\cos 2\gamma\rangle,$$

Additional moments which depend on the invariant masses s_1 and s_2 were proposed in [8] but, being less sensitive and strongly correlated with the other two, the reduction in the statistical error was small, while potential systematic errors introduced by the model were larger.

Fits to each of the distributions have been performed, always finding consistent values, thus allowing cross-checks of the fitting procedure.

The polarisation $\mathcal{P}_\tau$ was fitted in each of the six bins of cosΘ as described in Section 2. The results are shown in Table 2. The extraction of the electroweak parameters from these numbers is described in Section 9.2 and results are given in Table 9

The data for the two moments, summed over all cosΘ bins, are shown in Fig. 12.

The method used for measuring $\mathcal{P}_\tau$ relates the various components of the hadronic current. Thus, particular care should be taken in understanding possible biases due to the model dependence of the hadronic structure functions W_X. The effects of changing the Breit-Wigner parameters, of using different theoretical models [22–24] and of the possible presence of a scalar contribution have been investigated. However, it was found that the model dependence was marginal when the moments based on s_1 and s_2 were not included. The uncertainty in $\langle\mathcal{P}_\tau\rangle$ arising from the theoretical modelling of a_1 decays

was estimated to be 0.0015, by comparing the results using the different models. Other systematic errors in $\langle \mathcal{P}_\tau \rangle$ were: the γ reconstruction efficiency and fake γ misidentification probability estimation (0.024); other selection cuts (0.016) mainly from the VD association efficiency uncertainty; the momentum scale and resolution (0.013) and the finite simulation statistics (0.012). The uncertainty due to the acceptance in $\cos\theta_h$ was found to be negligible. The total systematic uncertainty was 0.033 and the main contributions are summarised in Table 3.

	$\tau \to e\nu\bar{\nu}$	$\tau \to \mu\nu\bar{\nu}$ (br.)	$\tau \to \mu\nu\bar{\nu}$ (fw.)	$\tau \to \pi(K)\nu$	$\tau \to \rho\nu$	$\tau \to 3\pi^{\pm}\nu_\tau$
e id./rej.	0.025	–	–	0.007	–	–
μ id./rej.	–	0.005	0.020	0.017	–	–
γ and π^0 id./rej.	–	–	–	0.010	0.009	0.024
external back.	0.025	0.008	0.020	0.002	–	–
energy scale/resol.	0.030	0.009	0.009	–	0.011	0.013
simulation stat.	0.013	0.009	0.016	0.007	0.006	0.012
others	–	–	–	0.001	0.008	0.016
total	0.048	0.018	0.033	0.022	0.017	0.033

Table 3: Summary of the main contributions to the systematic error for the exclusive channels for 1993 to 1995 data. The two columns for the $\tau \to \mu\nu\bar{\nu}$ channel correspond to barrel and forward analyses.

7 Inclusive $\tau \to$ one-prong hadronic decay

The highest sensitivity to the τ polarisation is obtained in the decays to $\pi\nu$ and $\rho\nu$. The identification of these channels however requires stringent cuts in order to avoid background contamination, mostly due to hadronic decays with more π^0's.

An inclusive measurement was made of the polarisation for decays to a single charged hadron with or without accompanying π^0's. This increased the selection efficiency, at the expense of a somewhat lower sensitivity per decay to the polarisation. Hemispheres with only one charged particle (after the γ conversion reconstruction) were accepted. The track had to lie in the polar angle range $|\cos\Theta| < 0.73$ or $0.8 < |\cos\Theta| < 0.94$. Furthermore, the extrapolation of the τ decay track to the HPC had to lie more than 0.5° away from any azimuthal boundary region of the HPC as the HPC response to electrons near these regions was degraded, rendering electron rejection more difficult.

The analysis was performed as a function of the hadronic invariant mass, m_h, computed from the charged particle track and all photons in a cone of half angle 30° about the track. It was assumed that the charged particle had the mass of a pion. For identification purposes, the data were separated in two regions of hadronic mass: $m_h < 0.3$ GeV/c^2, and 0.3 GeV/c^2 $< m_h <$ 1.9 GeV/c^2. These regions correspond to the dominant decay being $\pi\nu$ with no π^0's produced or $\rho\nu$ and $a_1\nu$ with one or several π^0's.

The first stage of electron rejection was performed using the dE/dx of the TPC. In the barrel region, it was required that $\Pi^{\pi}_{dE/dx} < 2$. This cut was particularly important in the low momentum region. Additional cuts described below, dependent on the hadronic invariant mass, were performed to further reduce the backgrounds.

- Decays with low hadronic mass were more heavily contaminated by muons and electrons. In the region $m_h < 0.3$ GeV/c^2, the hadron identification criteria were

tighter. To reject electrons, it was required that the associated electromagnetic energy deposited in the first 4 layers of the HPC be less than 2 GeV, or that there be associated energy in the HCAL beyond its first layer. The momentum of the single charged particle had to be greater than $0.037 \times p_{beam}$ to ensure that it had sufficient momentum to reach the muon chambers or at least the outer part of the HCAL, thus enabling efficient rejection of muon background. Muons were rejected by requiring that E_{hlay} be greater than 2 GeV or E_{hlay} was zero and that there be no hit in the muon chambers. In the regions which were not covered by the muon system, the muon veto was complemented with the requirement of no associated energy in the two outer HCAL layers.

- In the region $0.3\ \mathrm{GeV/c^2} < m_h < 1.9\ \mathrm{GeV/c^2}$, the background from muons was small enough not to require additional suppression. To reject electrons it was required that the electromagnetic energy deposited in the first 4 layers of the HPC be less than 5 GeV, or that there be associated energy in the HCAL beyond its first layer.

In the forward region the dE/dx cut was tightened to $\Pi^{\pi}_{dE/dx} < 1.5$ and the different cuts on the energy deposition on the first 4 layer of the HPC were replaced by a requirement $E_{EMF}/p < 0.6$.

In order to reduce the contamination from $\mu^+\mu^-$ and e^+e^- events further it was required that there be no single particle in the opposite hemisphere with momentum or electromagnetic energy greater than $0.85 \times E_{beam}$ (tightened in the forward region to $p < 0.8 \times E_{beam}$ and $E < 0.7 \times E_{beam}$).

The sample remaining after the cuts contained 54080 τ decays, selected with an efficiency of 66.5% within the angular acceptance. The background consisted of 3.0% from other τ decays and 1.1% from non-τ sources. The distribution of the hadronic mass is presented in Fig. 13 for the barrel candidates. Table 4 shows the sample composition as estimated by simulation, for the three main signal channels and backgrounds, as a function of the invariant mass. The average efficiency for hadronic channels is 76%. The efficiencies for the $\pi\nu$ and $\rho\nu$ channels are 75% and 83% respectively, much higher than for the exclusive analyses where more stringent cuts were made to remove the $\rho\nu$ and $a_1\nu$ decays, respectively.

Mass range	N_{data}	Signal channels			Background channels	
$[\mathrm{GeV/c^2}]$		$\pi\nu$	$\rho\nu$	$a_1\nu$	Other τ decays	Non τ decays
0.00-0.30	15466	68.4	21.1	3.2	5.6	1.9
0.30-0.55	5608	7.0	69.3	14.2	8.7	1.0
0.55-0.70	8564	1.8	79.9	14.2	3.8	0.5
0.70-0.85	10333	1.0	77.5	17.8	3.5	0.3
0.85-1.05	7149	1.4	56.6	35.6	5.7	0.7
1.05-1.30	4459	2.0	36.1	50.1	11.0	0.7
1.30-1.90	2501	4.6	32.5	44.2	16.8	2.0

Table 4: Number of selected decays and expected composition of the main channels in percentages in each mass range of measured mass for the one prong inclusive analysis. The sixth and seventh columns show the percentage of the data sample estimated to come from other tau decays or from non-tau backgrounds.

The polarisation was estimated using a 3-dimensional fit to the variables M_h, $\cos\theta_h$, and $\cos\psi_h$, which is closely related to the emission angle of the charged pion in the

hadronic rest frame (as described in Eq. 10):

$$\cos\psi_h = \frac{E_{ch} - E_{neu}}{E_{ch} + E_{neu}}, \tag{15}$$

where E_{ch} is the energy of the charged particle in the decay calculated using the measured momentum and the π mass, and E_{neu} is the neutral energy in a cone of half-angle of 30° about the charged particle. The invariant mass range was split into seven non uniform bins (as in table 4) chosen to be more sensitive to the different resonances in the sample. In the first mass bin $\cos\psi_h$ was not used, since π decays are the dominant source in this bin for which $\cos\psi_h$ has no significance.

The polarisation, $\mathcal{P}_\tau$, was fitted in each of the eight bins of cosΘ as described in Section 2. The results are shown in Table 2. The extraction of the electroweak parameters from these numbers is described in Section 9.2 and results are given in Table 9

The distributions of $\cos\theta_h$ and $\cos\psi_h$, summed over all cosΘ bins, are displayed in Fig. 14, with the simulated distributions for the fitted value of $\langle\mathcal{P}_\tau\rangle$ superimposed.

The momentum dependent efficiency for hadrons surviving the muon and electron rejection cuts was estimated using test samples of pions as explained in Section 6.3. In an analogous manner, test samples were used to estimate the uncertainty due to background from other τ decays.

The knowledge of the γ reconstruction efficiency, limited by the loss of neutral showers in the HPC due to threshold effects and dead space, was responsible for an additional uncertainty. The loss of photons causes migration of ρ and a_1 to lower invariant mass bins, distorting the measured polarisation. The neutral reconstruction efficiency in τ decays was known to better than 4%, from the comparison of different γ related distributions like those shown in Fig. 3. An extra loss of this amount was forced in the simulation and the variation of the result was taken as systematic error.

The branching ratios of the $\pi\nu$, $\rho\nu$ and $\pi\pi^0\pi^0\nu$ decay modes of the τ were varied by the uncertainties in the world average values in [25] and its effect on the measurement was included in the systematic error.

A shower from a π^0 or photon could accidentally be associated to the charged particle, causing the variables used in the analysis to be mismeasured. This was studied by adding the full energy associated to the charged track in the HPC into the neutral cone energy in the definitions of $\cos\theta_h$ and $\cos\psi_h$. The change in the measured polarisation was negligible in the overall fit and in each mass bin.

The uncertainty in knowledge of the external background was also propagated to the polarisation measurement. For the forward region this contribution was important due to the increase of the Bhabha scattering cross section.

The uncertainty due to radiative corrections in the τ decay processes was estimated in the manner described in Section 6.3 and 6.4.

Other important contributions to the systematic error were the effect on the measurement of the momentum and energy scales and resolution.

The uncertainties are listed in Table 5. The total systematic uncertainty in the combined value of $\langle\mathcal{P}_\tau\rangle$ was 0.0065 in the barrel and 0.014 in the forward region.

8 Neural network selection

In addition to the previously described exclusive and inclusive measurements a different approach using neural network techniques was used. All one prong decays were classified into five categories (e, μ, π, ρ and a_1) using a neural network. A polarisation estimator

Systematic source	barrel	forward
Simulation statistics	0.0025	0.008
electron/muon rejection	0.0036	0.007
γ efficiency	0.0020	0.002
τ branching ratios	0.0024	0.002
Non-τ background	0.0011	0.008
neutral energy scale and reso.	0.0029	0.003
momentum scale and reso.	0.0018	0.002
Radiative corrections	0.001	0.001
Total	0.0065	0.014

Table 5: Systematic errors in $\langle \mathcal{P}_\tau \rangle$ for the inclusive hadronic analysis.

was built as defined in Section 2 according to the assigned class: the momentum for leptonic decays, $\cos\theta_h$ for the π, and two-dimensional distributions of $\cos\theta$ versus $\cos\psi$ for the ρ and a_1. A simultaneous fit of the five data distributions to a linear combination of simulated $+1$ and -1 polarisation distributions was performed.

Neural networks optimise the statistical discrimination of multidimensional variables for non linear problems, including correlations of the variables. This is especially useful for the discrimination of hadronic decays, where the separation comes from the relationship of several variables, each of them having small sensitivity.

A feed-forward neural network was used [26]. The network was fed with eleven discriminant variables as input:

- Momentum of the charged particle,
- $\Pi_{dE/dx}$ for electron hypothesis as defined in Section 6.1,
- $\Pi_{E/p}$ for electron hypothesis as defined in Section 6.1,
- Fraction of energy deposited in the first four layers of the HPC by the charged particle, A_{em},
- Number of hits in the muon chambers associated to the charged particle,
- Average HCAL energy as defined in Section 6.1, E_{hlay},
- Fraction of energy deposited in the last two layers of the HCAL, A_{had},
- Number of photons counting the showers identified as coming from a π^0 as two,
- Total invariant mass,
- Invariant mass of the neutrals,
- Neutral energy in the electromagnetic calorimeters.

The neural network was created using the SNNS [27] software package. Different network architectures (varying numbers of hidden layers and neurons in the hidden layers) were tested to find the simplest network providing the best separation on simulated test samples. A network with three fully connected layers was chosen with the following characteristics:

- input layer with 11 neurons, corresponding to the 11 variables characterising the decay described above,
- one hidden layer with 7 neurons,
- one output layer with 5 neurons whose values could vary between 0 and 1, each neuron corresponding to one of the five categories into which the decay can be classified.

The weights or importance of the connections were optimised with a training procedure performed using a sample of 7500 simulated decays with 1500 in each class. The training consisted in minimising, as a function of the weights, the Euclidean distance of the five output values to the known truth (1 for the neuron corresponding to the known decay and 0 for all other neurons). Therefore the output values tended to be close to 1 for one output neuron and to 0 for the remaining ones. The minimisation is done using the method of back-propagation with the gradient descent [26].

The decays were classified following the "winner rule", i.e. according to the neuron whose output is maximum, but other methods were tested and are discussed below. Samples of positive and negative helicity simulated tau decays were passed through the network to estimate backgrounds and selection efficiencies. These samples were independent of the training sample to avoid overtraining. Table 6 shows the probability, with respect to the preselected event sample, of assigning a given channel to a given class as estimated by the simulation after the corrections discussed in previous sections. Table 7 shows the purity and number of selected hemispheres in each class. The use of the neural network provided an optimal separation of the five channels for the 11 variables chosen, increasing the selection efficiency of the linear cut selections while keeping similar background levels.

	Probability of classification (%)				
assigned class / generated decay	$\tau \to e\nu_e\nu_\tau$	$\tau \to \mu\nu_\mu\nu_\tau$	$\tau \to \pi/K\nu_\tau$	$\tau \to \rho\nu_\tau$	$\tau \to a_1\nu_\tau$
$\tau \to e\nu_e\nu_\tau$	**95.86±0.05**	0.09±0.01	2.34±0.04	1.56±0.03	0.15±0.01
$\tau \to \mu\nu_\mu\nu_\tau$	0.07±0.01	**97.05±0.04**	2.56±0.04	0.29±0.01	0.03±0.01
$\tau \to \pi\nu_\tau$	3.73±0.05	2.81±0.05	**84.79±0.10**	7.46±0.07	1.21±0.03
$\tau \to \rho\nu_\tau$	1.68±0.03	0.60±0.02	8.16±0.05	**79.91±0.08**	9.65±0.06
$\tau \to a_1\nu_\tau$	1.05±0.04	0.19±0.02	1.83±0.05	40.79±0.17	**56.14±0.17**
$\tau \to K\nu_\tau$	0.25±0.05	2.38±0.16	**88.90±0.34**	7.59±0.28	0.87±0.10
other 1-prong	1.89±0.07	0.90±0.05	17.04±0.19	39.66±0.25	40.50±0.25

Table 6: Efficiency matrix for the neural network classification. Each row represents the probabilities to classify a given decay in each of the categories (defined with respect to the sample of preselected events).

τ decay mode	Number selected decays	Purity of the samples (%)
$\tau \to e\nu_e\nu_\tau$	18434	89.4 ± 0.1
$\tau \to \mu\nu_\mu\nu_\tau$	19811	94.3 ± 0.1
$\tau \to \pi/K\nu_\tau$	14850	73.2 ± 0.1
$\tau \to \rho\nu_\tau$	26548	75.4 ± 0.1
$\tau \to a_1\nu_\tau$	9446	53.2 ± 0.2

Table 7: Number of decays and purity (estimated from the simulation and using the world-average values for the τ decay branching ratios) in each channel for the selection of the exclusive $1-prong$ τ decay channels with a neural network.

The polarisation $\mathcal{P}_\tau$ was fitted in each of the six bins of cosΘ as described in Section 2. The results are shown in Table 2. The extraction of the electroweak parameters from these numbers is described in Section 9.2 and results are given in Table 9

The systematic errors were estimated in a similar way to the standard cuts analyses. The detector response was compared in real data and simulated test samples selected independently, and all discrepancies or corrections in variables related to the inputs were propagated through the network to the results. The momentum and energy scales were treated similarly. The network stability was checked, by repeating the training several times and changing the classification procedure: events were classified in a given class if the corresponding neuron had a value larger than 0.5[1]. Both methods gave compatible results. The possible bias on the polarisation induced by the experimental precision in the branching ratios was estimated repeating the fit with these branching ratios as free parameters (in addition to $\langle\mathcal{P}_\tau\rangle$) fitting them from the relative amount of data in each class. The total systematic uncertainty was 0.0061, with the main sources listed in Table 8.

Systematic source	$\Delta\langle\mathcal{P}_\tau\rangle$
Simulation statistics	0.0031
muon ID	0.0015
electron ID	0.0020
Neutral energy scale and resol.	0.0027
momentum scale and resol.	0.0019
γ efficiency	0.0024
τ branching ratios	0.0017
Non-τ background	0.0007
Radiative corrections	0.001
Total	0.0061

Table 8: Systematic errors in $\langle\mathcal{P}_\tau\rangle$ for the neural network analysis.

9 Extraction of $\mathcal{A}_\tau$ and $\mathcal{A}_e$

9.1 Method

To determine $\mathcal{A}_\tau$ and $\mathcal{A}_e$, the average polarisation, $\langle\mathcal{P}_\tau\rangle$, was measured as a function of the polar angle Θ as summarised in Tables 1 and 2. A fit to the theoretical expectation in terms of $\mathcal{A}_\tau$ and $\mathcal{A}_e$ was performed. In the previous analyses [5,6], the Born level equivalence $\frac{4}{3}A_{FB} = \mathcal{A}_\tau \cdot \mathcal{A}_e$ was used in the formula in equation 3, a simultaneous fit to $\mathcal{A}_\tau$ and $\mathcal{A}_e$ was performed and the values obtained were corrected accounting for effects such as the QED contribution, radiation or centre-of-mass energy dependence. This correction was $\mathcal{O}(0.005)$ for both $\mathcal{A}_\tau$ and $\mathcal{A}_e$. However, it was found that this procedure was not ideal for the precision required with the present data, because firstly the above factorisation is not a good approximation after radiative corrections and secondly, because A_{FB} has a strong centre-of-mass energy dependence. The offset induced on $\mathcal{A}_\tau$ and $\mathcal{A}_e$ is of the order of 0.001 on the Z peak, but can be as large as 0.030 for $\mathcal{A}_e$ in the off-peak points,

[1] a small fraction of the events were not selected by this procedure and as a consequence it gave slightly better purity than the "winner rule" for slightly lower efficiencies

although the smaller amount of data off-peak and the partial cancellation of higher and lower energies make the effect on the global result much smaller. To avoid any possible bias from this source a more precise approach was used. The fit was performed using as an estimation of $\mathcal{P}_\tau(\cos\Theta)$ the ZFITTER [28] prediction averaged in $\cos\Theta$ over the bin width and the centre-of-mass energies (weighted by the corresponding luminosities). This automatically included QED and weak effects. As a consequence, the fitted values were the polarisation parameters $\mathcal{A}_\tau$ and $\mathcal{A}_e$ defined in equations 1 and 2 in terms of the improved Born couplings. The uncertainty in the top quark mass and the unknown Higgs boson mass had a negligible effect.

9.2 Results

The average polarisation in each channel was obtained as a function of $\cos\Theta$, as explained in Sections 6, 7 and 8. The results are shown in Tables 1 and 2, both for the new analyses of 1993 to 1995 data and for those already published for 1991 and 1992 [5]. To account for the common systematic between the new and published data and for the new approach for the theoretical expectation the following procedure was followed:

- new and published average polarisations values were combined for each channel and for each $\cos\Theta$ bin
- $\mathcal{A}_\tau$ and $\mathcal{A}_e$ were fitted from the $\cos\Theta$ dependence for each channel
- the values for $\mathcal{A}_\tau$ and $\mathcal{A}_e$ for all channels were combined together and with the 1990 result (which was not analysed in terms of $\cos\Theta$).

All available data (new and published) for a given channel and a given $\cos\Theta$ were combined together taking into account systematic correlations. The result of this combination is also shown in Tables 1 and 2. The consistency between results was good, a χ^2 of 43 for 36 d.o.f. (probability of 20%) was found for the combination.

The average polarisation as a function of the polar angle was then fitted to the ZFITTER theoretical expectation and $\mathcal{A}_\tau$ and $\mathcal{A}_e$ were obtained for each analysed channel. These results are shown in Table 9. The fact that most of the systematic errors described in the previous section were totally correlated between different bins in $\cos\Theta$ was taken into account. This had the effect that the error propagated by the fit to $\mathcal{A}_\tau$ was essentially the quoted error on $\langle\mathcal{P}_\tau\rangle$. On the contrary this had a negligible effect on $\mathcal{A}_e$, because to first order $\mathcal{A}_e$ is calculated from the difference of $\langle\mathcal{P}_\tau\rangle$ between bins symmetric with respect to $\cos\Theta = 0$ and therefore there is a cancellation of those systematic errors that are correlated between bins.

For equivalent reasons, other systematic uncertainties in the polarisation affect $\mathcal{A}_e$ if they are forward-backward asymmetric and charge dependent. An example is the track curvature in the TPC, which can be offset by detector effects differently for opposite hemispheres, causing different charge-dependent losses in sector boundaries of the TPC for positive and negative z. This, however, was estimated to have negligible effect on $\mathcal{A}_e$. Misidentification of the τ charge from its decay products was estimated on data to be $0.45 \pm 0.15\%$. The choice of the decay product polar angle, rather than that of the τ, smears the $\cos\Theta$ distributions. A similar but smaller effect was produced by the resolution and calibration of Θ. From the approximate formula 3 and neglecting quadratic terms in $\mathcal{A}$, it was found that all these effects produced a reduction in $\mathcal{A}_e$, which was proportional to the r.m.s. of the difference between the real and estimated polar angles. From the charge misidentification, estimated from data, and the Θ resolution (including both detector effects and the assumption that the decay product reproduces the τ direction), estimated from simulation, this effect was found to be $1.2 \pm 0.4\%$. Therefore, $\mathcal{A}_e$ was corrected with

a multiplicative factor of 1.012 and a contribution of $0.004\mathcal{A}_e$ was added to its systematic uncertainty.

The fact that some of the errors depended on Θ, non-tau background or identification in the end-caps, was also considered. In all cases their contribution to $\mathcal{A}_e$ systematic error was negligible, although the central values of $\mathcal{A}_e$ and $\mathcal{A}_\tau$ were affected due to the change in the relative weights of the different measurements.

Channel	$\mathcal{A}_\tau$	$\mathcal{A}_e$	χ^2
$\tau \to e\nu\bar{\nu}$	$0.166 \pm 0.038 \pm 0.042$	0.182 ± 0.058	4.2/4
$\tau \to \mu\nu\bar{\nu}$	$0.149 \pm 0.029 \pm 0.020$	0.106 ± 0.039	6.7/6
$\tau \to \pi(\mathrm{K})\nu$	$0.187 \pm 0.020 \pm 0.022$	0.127 ± 0.031	11.7/4
$\tau \to \rho\nu$	$0.116 \pm 0.019 \pm 0.016$	0.143 ± 0.028	6.5/4
$\tau \to a_1\nu$	$0.133 \pm 0.034 \pm 0.032$	0.162 ± 0.050	0.9/4
Inclusive	$0.1268 \pm 0.0091 \pm 0.0070$	0.1400 ± 0.0131	5.3/6
Neural net	$0.1348 \pm 0.0123 \pm 0.0061$	0.1369 ± 0.0183	0.6/4

Table 9: Fit results for individual channels (91 to 95 data). Uncertainties are statistical followed by systematic for $\mathcal{A}_\tau$ and only statistical for $\mathcal{A}_e$ (all channels had a 0.0005 correlated systematic error). The last column shows the χ^2 and degrees of freedom of the fit.

The fitted results of $\mathcal{A}_\tau$ and $\mathcal{A}_e$ per channel were combined together and with the 1990 result [4] of $\mathcal{A}_\tau = 0.24 \pm 0.07$, where the analysis was not performed in terms of $\cos\Theta$. The statistical correlations between the measurements obtained with the different analyses are summarised in Table 10. These were found by estimating the sensitivity to the polarisation and the number of decays contained in the overlaps of the samples. For the inclusive hadronic and neural network analyses the samples used correspond to the full results, rather than the subsamples corresponding to different exclusive decay modes. The correlation in the systematic errors between channels was taken into account in the combination. The statistical error of the simulation was combined with the same correlation coefficients as the data. The errors arising from the limited statistics in data samples for data/simulation comparisons (particle identification and energy and momentum scale and resolution) were treated as fully correlated when the same data sample was used and as completely independent otherwise. The error produced by the external background was also considered as fully correlated when it was caused by the same type of process.

The results were:

$$\mathcal{A}_\tau = 0.1359 \pm 0.0079 \pm 0.0055, \qquad \chi^2 = 7.4/7,$$

$$\mathcal{A}_e = 0.1382 \pm 0.0116 \pm 0.0005, \qquad \chi^2 = 1.6/6$$

and assuming leptonic universality:

$$\mathcal{A}_l = 0.1368 \pm 0.0065 \pm 0.0035, \qquad \chi^2 = 9.0/13$$

where the first error is statistical and the second systematic. The χ^2 reflects the consistency of the different measurements. The statistical error has been multiplied by a factor 1.02 to take account of the anticorrelation of the τ^+ and τ^- helicities in an event and the consequent underestimation of the statistical error in events where both τ^+ and τ^- where

analysed. This effect was estimated on simulation and accounted for the fraction of events where both τ^- and τ^+ were analysed as well as for the sensitivity to the polarisation of each decay. The correlation between the values of $\mathcal{A}_\tau$ and $\mathcal{A}_e$ was 0.03.

Channels	Inclusive	Neural Network
$\tau \to e\nu\bar{\nu}$	-	0.05
$\tau \to \mu\nu\bar{\nu}$	-	0.04
$\tau \to \pi(\mathrm{K})\nu$	0.2	0.4
$\tau \to \rho\nu$	0.5	0.5
Inclusive	1	0.7

Table 10: Statistical correlation between measurements for 1993 to 1995 data (negligible if not mentioned).

Another approach, equivalent statistically, which provided additional information of the compatibility of the different analyses was also used. In each cosΘ bin the average polarisation for all channels (new and published data) were combined taking into account the statistical and systematic correlations. The results are shown in Table 11 and in Fig. 15. The χ^2 of the combination was 50.7 for 38 d.o.f. (8% probability), indicating again that the different channels gave compatible results, not only in the fitted parameters but also in their cosΘ dependence. The parameters were fitted in the same way as before, giving the same results within numerical round-offs. The χ^2 of the fit was 5.7 for 6 d.o.f.

$\cos\Theta$	$\mathcal{P}_\tau$	χ^2/d.o.f.
-0.940,-0.732	-0.012 ± 0.043	0.6/1
-0.732,-0.488	-0.025 ± 0.020	5.5/6
-0.488,-0.244	-0.021 ± 0.021	10.0/6
-0.244, 0.000	-0.116 ± 0.023	8.5/6
0.000,$+0.244$	-0.147 ± 0.023	15.6/6
$+0.244$,$+0.488$	-0.223 ± 0.020	6.8/6
$+0.488$,$+0.732$	-0.259 ± 0.020	3.1/6
$+0.732$,$+0.940$	-0.199 ± 0.043	0.2/1

Table 11: τ polarisation values in bins of cosΘ for the combination of all analyses 1991 to 1995 data. The errors are statistical and systematic combined in quadrature. The final column shows for each bin the χ^2 of the combination.

It was checked that both central values and errors did not depend strongly on the correlation coefficients. The numbers were stable under absolute modifications of ± 0.2 in these coefficients. The inclusion of several channels with strong correlations, namely the inclusive and neural network analyses, does not affect the final result significantly. Removing the neural network analysis or the inclusive analysis does not produce a significantly different result. Moreover, this redundancy constitutes a cross-check for the measurements, since inconsistencies would be reflected in a poor χ^2.

Although after the different fits, the different sources of systematic errors on $\mathcal{A}_\tau$ are not well defined, an attempt was made to estimate the main contributions to the overall result. The complete procedure was repeated neglecting a given error source, and the

quadratic difference of the errors with or without that source was taken as an estimate of the contribution of that source to the overall error. For $\mathcal{A}_e$ the correlation between systematic errors is almost 100% and therefore the contributions to the total error are equivalent to those described in the previous section. The main contributions for $\mathcal{A}_\tau$ and $\mathcal{A}_e$ are summarised in Table 12.

Systematic source	$\Delta\mathcal{A}_\tau$
Simulation statistics	0.0023
γ ID/ fake γ rejection	0.0028
Neutral energy scale	0.0012
momentum scale	0.0013
τ branching ratios	0.0016
Non-τ background	0.0013
leptonic ID/rejection	0.0026
others	0.0015
Systematic source	**$\Delta\mathcal{A}_e$**
τ charge	0.0005
τ direction	0.0002

Table 12: Contributions to the systematic errors in $\mathcal{A}_\tau$ and $\mathcal{A}_e$ for 1990 to 1995 data.

10 Summary and Conclusions

The polarisation of the τ and its polar angle dependence have been determined firstly through the study of exclusive decay channels, secondly from an inclusive analysis, and thirdly with a neural network selection. The results agree well with the results in our previous publication based on 1990 to 1992 data [5] and have thus been combined. The different measurements were found to be consistent with each other. They are summarised in Table 9. The polar angle dependence is displayed in Fig. 15 and in Table 11. The results were

$$\mathcal{A}_\tau = 0.1359 \pm 0.0079(stat) \pm 0.0055(sys)$$
$$\mathcal{A}_e = 0.1382 \pm 0.0116(stat) \pm 0.0005(sys)$$

From these results the ratios of the effective weak couplings of the τ and e are calculated to be:

$$\bar{v}_\tau/\bar{a}_\tau = 0.0683 \pm 0.0048,$$
$$\bar{v}_e/\bar{a}_e = 0.0694 \pm 0.0058,$$

supporting the hypothesis of lepton universality.

The assumption of lepton universality gives the results:

$$\mathcal{A}_l = \mathcal{A}_\tau = \mathcal{A}_e = 0.1368 \pm 0.0065(stat) \pm 0035(sys)$$

and the ratio of effective leptonic couplings,

$$\bar{v}_l/\bar{a}_l = 0.0687 \pm 0.0037,$$

leading to the result

$$\sin^2\theta^{\rm lept}_{\rm eff} = 0.23282 \pm 0.00092,$$

compatible with the values obtained from other measurements [6] of the τ polarisation at LEP and with an improved precision. The result is also compatible with other $\sin^2\theta^{\rm lept}_{\rm eff}$ measurements [29]. A significant improvement in the precision with respect to previous DELPHI results [5] has been achieved.

Acknowledgements

We are greatly indebted to our technical collaborators, to the members of the CERN-SL Division for the excellent performance of the LEP collider, and to the funding agencies for their support in building and operating the DELPHI detector.
We acknowledge in particular the support of
Austrian Federal Ministry of Science and Traffics, GZ 616.364/2-III/2a/98,
FNRS–FWO, Belgium,
FINEP, CNPq, CAPES, FUJB and FAPERJ, Brazil,
Czech Ministry of Industry and Trade, GA CR 202/96/0450 and GA AVCR A1010521,
Danish Natural Research Council,
Commission of the European Communities (DG XII),
Direction des Sciences de la Matière, CEA, France,
Bundesministerium für Bildung, Wissenschaft, Forschung und Technologie, Germany,
General Secretariat for Research and Technology, Greece,
National Science Foundation (NWO) and Foundation for Research on Matter (FOM), The Netherlands,
Norwegian Research Council,
State Committee for Scientific Research, Poland, 2P03B06015, 2P03B1116 and SPUB/P03/178/98,
JNICT–Junta Nacional de Investigação Científica e Tecnológica, Portugal,
Vedecka grantova agentura MS SR, Slovakia, Nr. 95/5195/134,
Ministry of Science and Technology of the Republic of Slovenia,
CICYT, Spain, AEN96–1661 and AEN96-1681,
The Swedish Natural Science Research Council,
Particle Physics and Astronomy Research Council, UK,
Department of Energy, USA, DE–FG02–94ER40817.

References

[1] Z Physics at LEP I, edited by G.Altarelli, R.Kleiss and C.Verzegnassi, CERN 89-08 (1989).

[2] OPAL Collaboration, K. Ackerstaff et al.,Eur. Phys. J. **C8** (1999) 1, 3-21;
L3 Collaboration, M. Acciari et al., Phys. Lett. **B438** (1998) 405;
CLEO Collaboration, J. Alexander et al., Phys. Rev. **D56** (1997) 5320;
SLD Collaboration, K. Abe et al.,Phys. Rev. Lett. **78** (1997) 4691;
ARGUS Collaboration, H. Albrecht et al., Phys. Lett. **B349** (1995) 576;
ALEPH Collaboration, D. Buskulic et al., Phys. Lett. **B346** (1995) 379.

[3] "A Study of the Lorentz Structure in Tau decays", DELPHI Collaboration, P.Abreu et al., to be submitted to Eur.Phys. J. C.

[4] DELPHI Collaboration, P.Abreu et al., Z. Phys. **C55** (1992) 555.

[5] DELPHI Collaboration, P. Abreu et al. , Zeit. Phys. **C67** (1995) 183.

[6] ALEPH Collaboration, D. Decamp et al., Phys. Lett. **B265** (1991) 430;
OPAL Collaboration, G. Alexander et al., Phys. Lett. **B266** (1991) 201;
L3 Collaboration, O. Adriani et al., Phys. Lett. **B294** (1992) 466;
ALEPH Collaboration, D. Buskulic et al., Z. Phys. **C59** (1993) 369;
L3 Collaboration, O. Adriani et al., Phys. Lett. **B341** (1994) 245;
OPAL Collaboration, R. Akers et al., Z. Phys. **C65** (1995) 1.
L3 Collaboration, M. Aciarri et al., Phys. Lett. **B429** (1998) 387

[7] M. Davier et. al., Phys. Lett. **B306** (1993) 411.
A. Rougé, Z. Phys. **C48** (1990) 75.

[8] P. Privitera, Phys. Lett. **B308** (1993) 163.

[9] B. K. Bullock, K. Hagiwara, A. D. Martin, Nucl. Phys. **B395** (1993) 499.

[10] J. H. Kühn, E. Mirkes, Phys. Lett. **B286** (1992) 381;
J. H. Kühn, E. Mirkes, Z. Phys. **C56** (1992) 661.

[11] S. Jadach et al., Comp. Phys. Comm. **79** (1994) 503;
S. Jadach et al., Comp. Phys. Comm. **70** (1992) 69.

[12] DELPHI Collaboration, Nucl. Instr. and Meth. **A378** (1996) 57-100.

[13] J. E. Campagne and R. Zitoun, Z. Phys. **C43** (1989) 469.

[14] F. A. Berends, W. Hollik and R. Kleiss, Nucl. Phys. **B304** (1988) 712.

[15] S.Jadach et al. Phys. Lett. **B390** (1997) 298.

[16] H.Anlauf et al, report IKDA 95/34, hep-ex/9512006 (unpublished)

[17] T.Sjöstrand, Comp. Phys. Comm. **27** (1982) 243, ibid. **28** (1983) 229;
T.Sjöstrand and M. Bengtsson, Comp. Phys. Comm. **43** (1987) 367;
T.Sjöstrand, "PYTHIA 5.6 JETSET 7.3 Physics and manual", report CERN-TH 6488/92 (1992).

[18] F.A.Berends, P.H.Daverveldt, R.Kleiss, Phys. Lett. **B148** (1984) 489;
Comp. Phys. Comm. **40** (1986) 271.

[19] DELPHI Collaboration, Nucl. Instr. and Meth. **A303** (1991) 233.

[20] DELPHI Collaboration, P. Abreu et al., Eur. Phys. J. **C10** (1999) 201.

[21] The LEP collaborations, "Combined Preliminary Data on Z Parameters from the LEP Experiments and Constraints on the Standard Model", report CERN/PPE/94-187, Nov 1994;
R. Decker and F. Finkemeier, Phys. Rev. **D48** (1993) 4203;
M. Finkemeier, "Radiative Corrections to the decay $\tau \to \pi\nu$", Doctoral thesis, University of Karlsruhe, February 1994.

[22] J. H. Kühn, A. Santamaria, Z. Phys. **C48** (1990) 445.

[23] N. Isgur, C. Morningstar, C. Reader, Phys. Rev. **D39** (1989) 1357.
[24] M. Feindt, Z. Phys. **C48** (1990) 681.
[25] Particle Data Group, C. Caso et al., Eur. Phys. J. **C3**, (1998) 1-794 .
[26] D.E.Rumelhart et al, Parallel Distributed Processing, Feldman, Hayes and Rumelhart edit., Vol. 1, p.318-362, MIT Press, Cambridge, 1986.
[27] A.Zell et al., Österrreich Artificial-Intelligence-Tagung, Wien 1991.
[28] D. Bardin et al., Z. Phys. **C44** (1989) 493;
D. Bardin et al., "ZFITTER: An Analytical Program for Fermion Pair Production in e^+e^- Annihilation", CERN-TH 6443/92 (1992).
[29] LEP collaborations, LEP E.W.G., SLD H.F.G and SLD E.W.G, CERN PPE 99–15

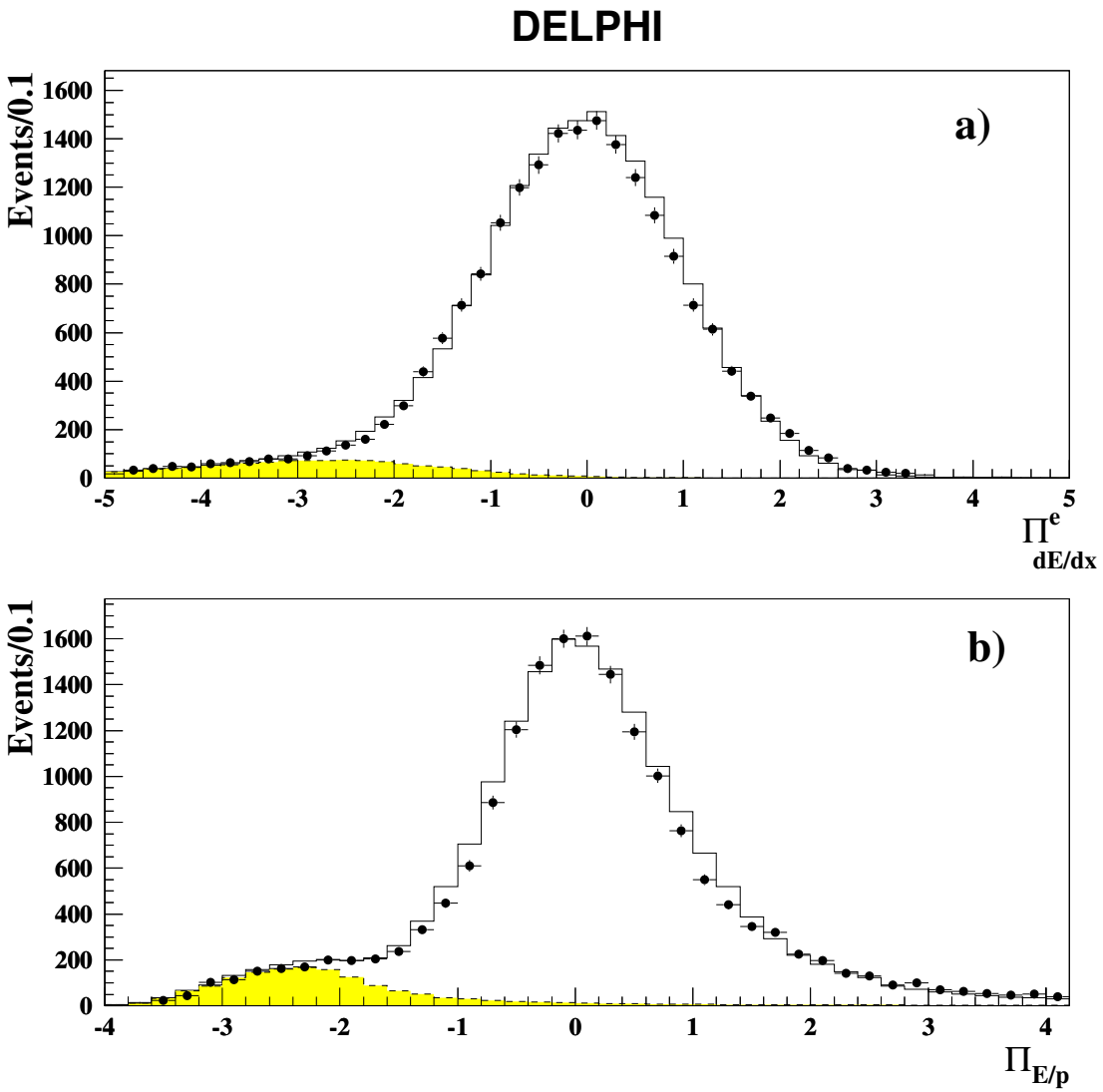

Figure 1: Distribution of electron identification variables for electron test samples: **a)** pull dE/dx and **b)** pull E/p for electron hypothesis. The solid line is for all simulation, the hatched area represents the background (anything except τ decays to electrons) and the circles are the data.

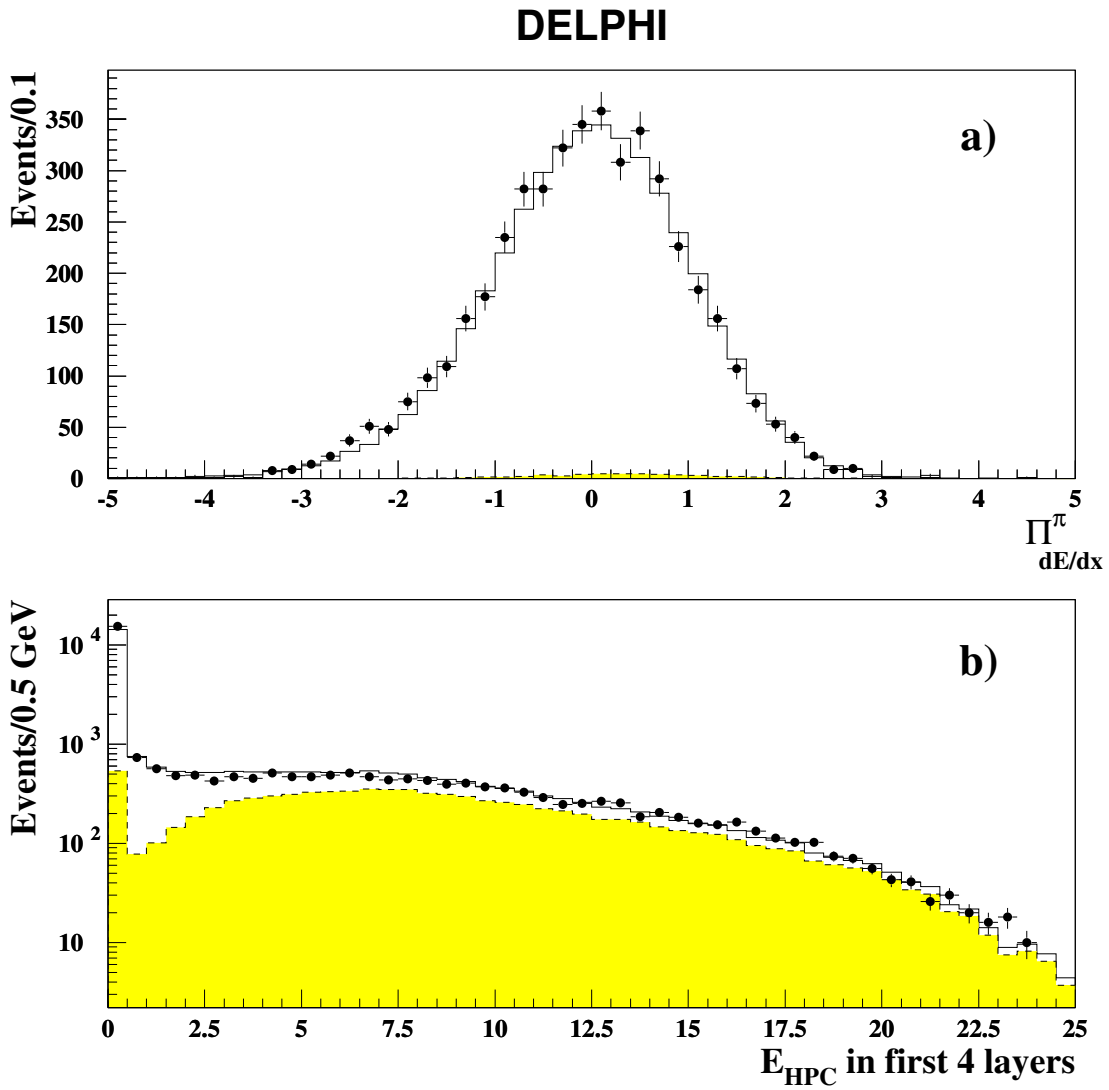

Figure 2: Distribution of hadron identification variables for charged hadrons from τ decays: **a)** pull dE/dx for π hypothesis and **b)** energy deposited in the first four layers of the HPC. Circles are data, the solid line is simulation and the hatched area represents the background (anything except τ decays to hadrons).

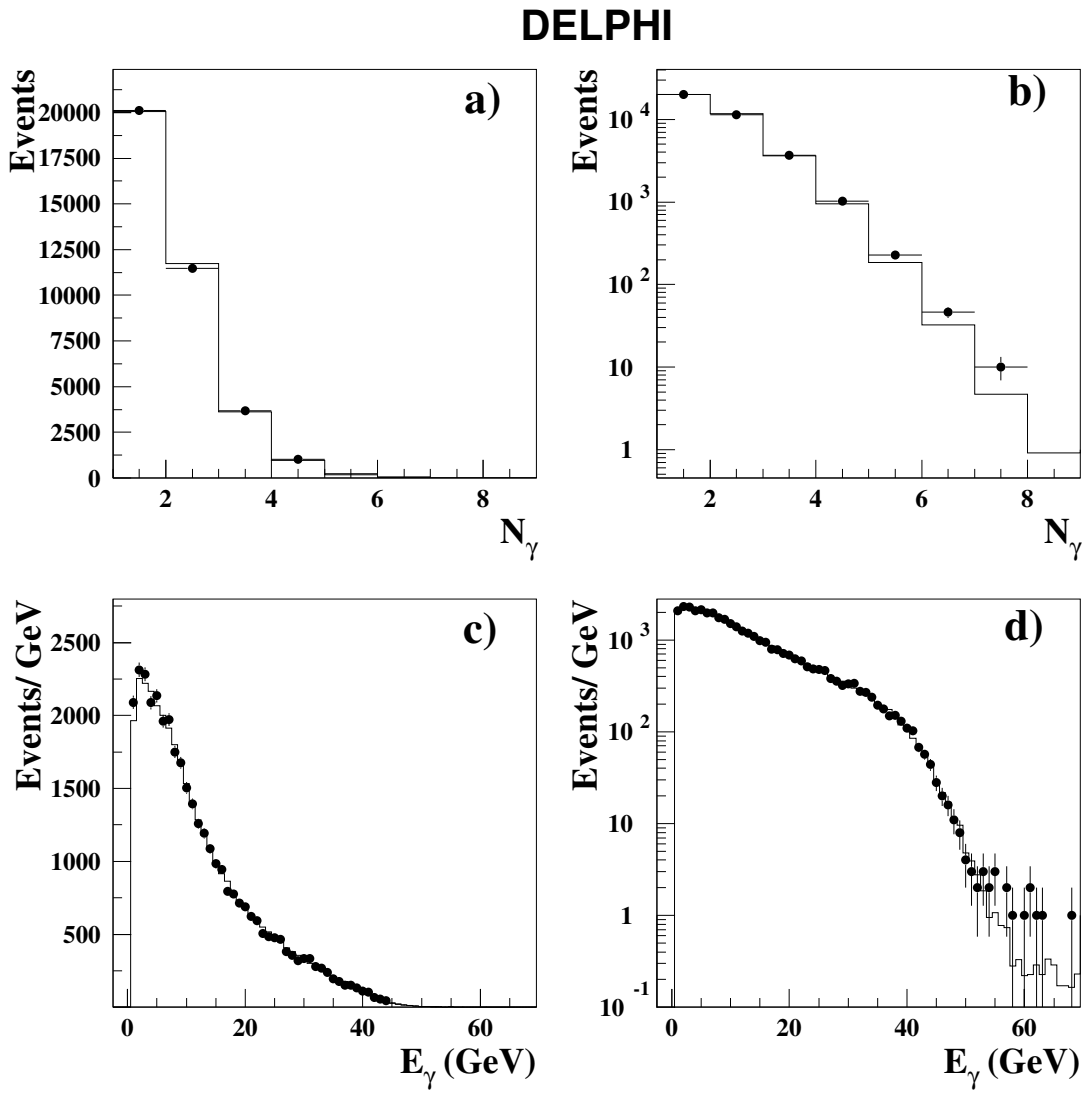

Figure 3: **a-b)** Neutral multiplicity and **c-d)** energy spectra for all identified γ for an inclusive τ sample. Left hand side plots are in linear scale and right hand side in logarithmic scale. Circles are data and the solid line is simulation.

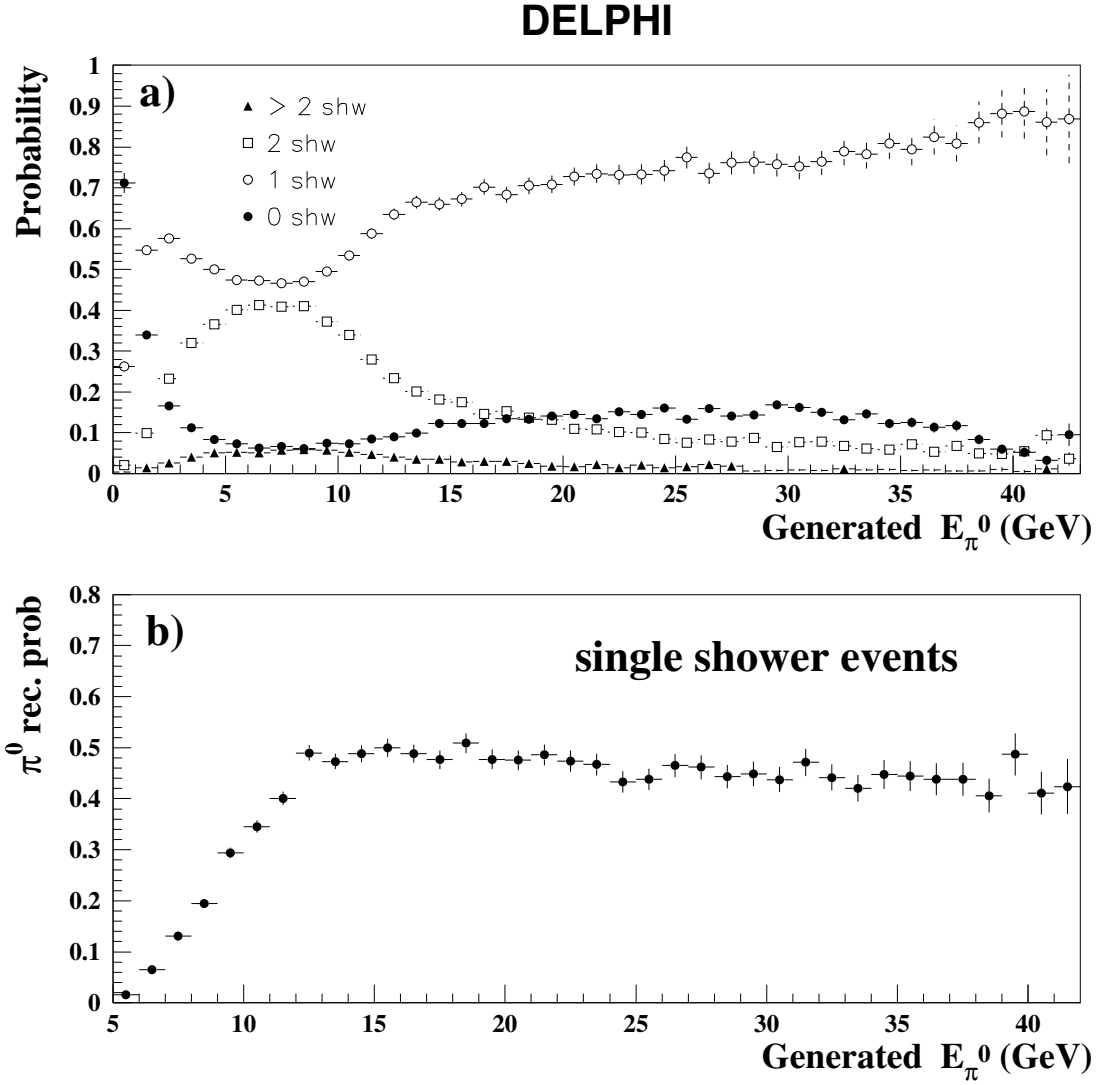

Figure 4: **a)**Probabilities of reconstructing a single π^0 as n showers or reconstructed photons from conversions as a function of π^0 energy for simulated ρ decays. Solid circles are for $n = 0$, open circles for $n = 1$, open squares for $n = 2$ and solid squares for more than 2. **b)**Probability that a single shower in the HPC is recognised as a π^0 as a function of π^0 energy for simulated ρ decays.

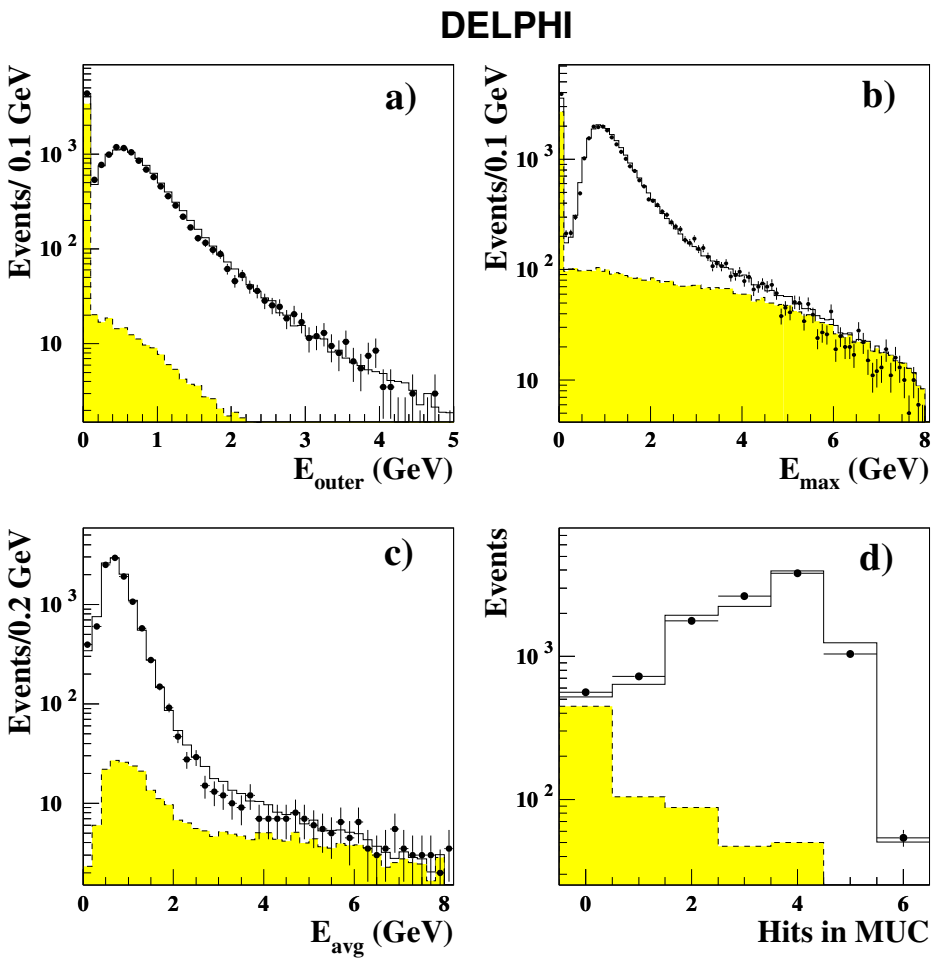

Figure 5: Distribution of muon identification variables for muon test samples. **a)** Energy in the outermost HCAL layer, **b)** largest HCAL energy deposition, **c)** average HCAL energy and **d)** muon chamber hits. Circles are data, the solid line is simulation and the hatched area represents the background (anything except τ decays to muons)

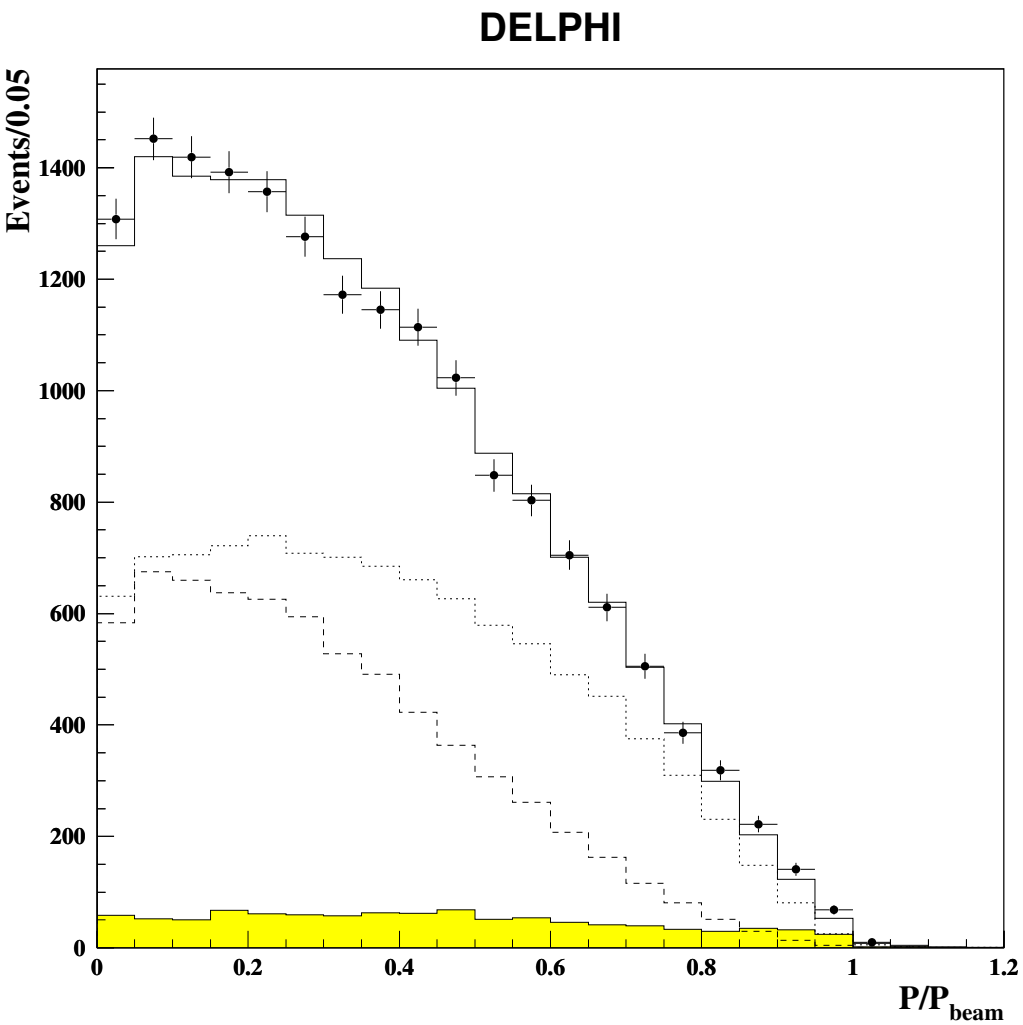

Figure 6: p_{el}/p_{beam} spectrum for candidate $\tau \to e\nu\bar{\nu}$ decays. The circles are data and the solid line is simulation for the fitted value of $\langle \mathcal{P}_\tau \rangle$. The hatched area is background and the dashed and dotted lines correspond to the positive and the negative polarisation contributions respectively.

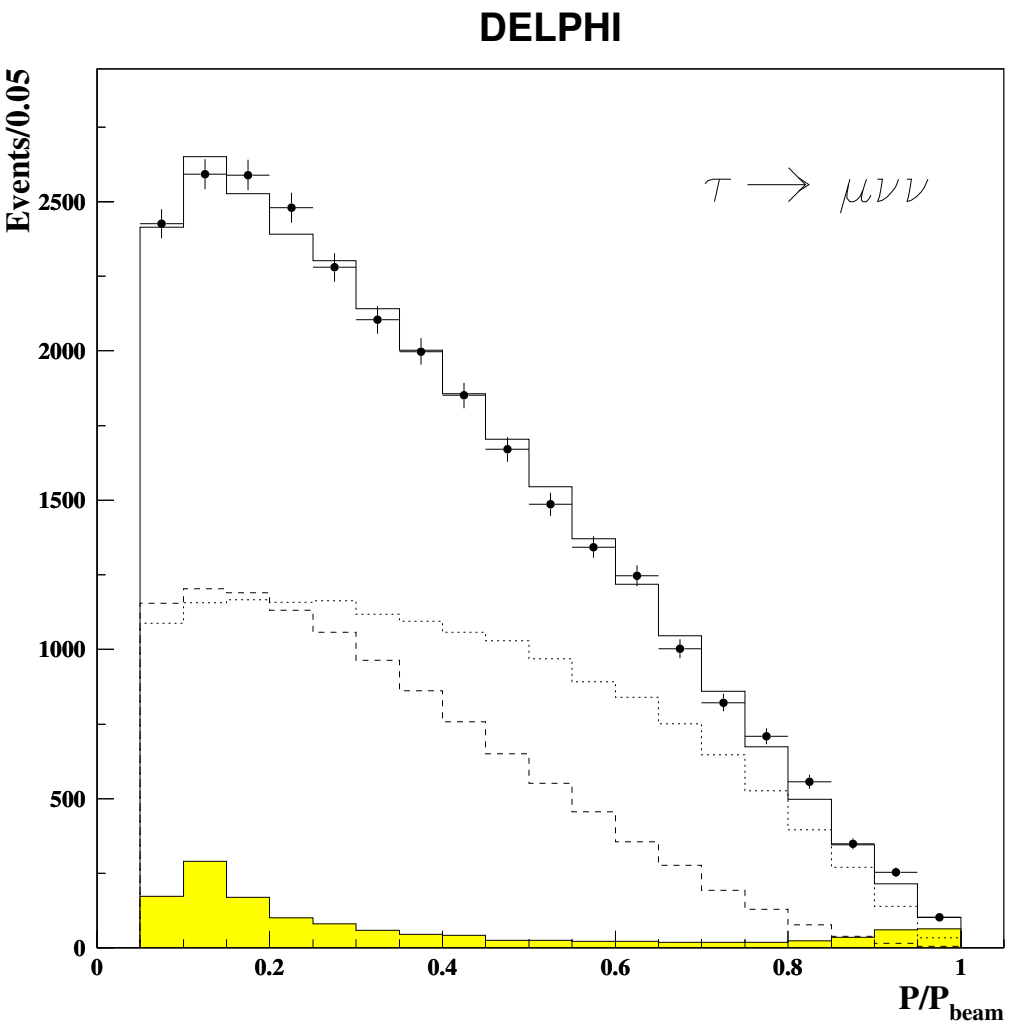

Figure 7: P/p_{beam} spectrum for candidate $\tau \to \mu\nu\bar{\nu}$ decays. The circles are data and the solid line is simulation for the fitted value of $\langle \mathcal{P}_\tau \rangle$. The hatched area is background and the dashed and dotted lines correspond to the positive and the negative polarisation contributions respectively.

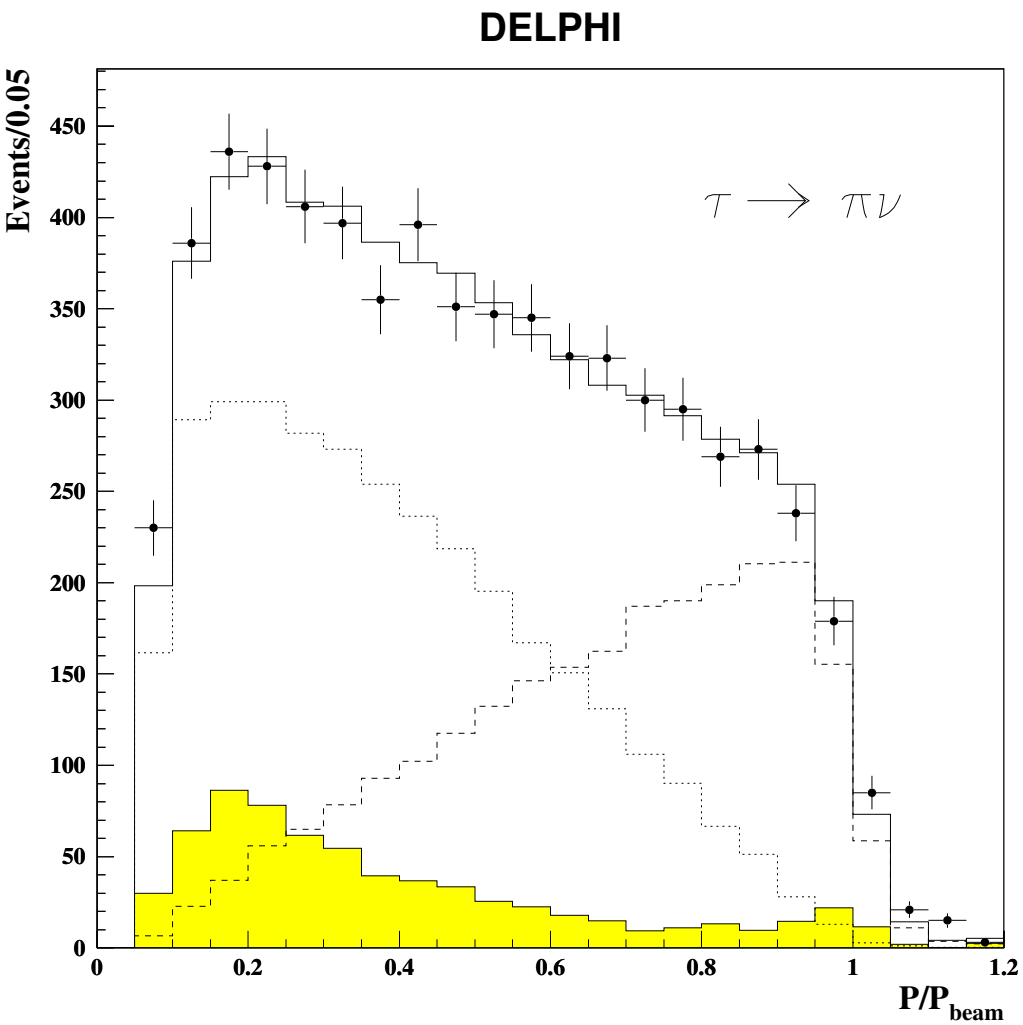

Figure 8: The spectrum, for $\tau \to \pi(\mathrm{K})\nu$ decays as a function of the $\pi(\mathrm{K})$ momentum normalised to the beam momentum. The circles are data and the solid line is simulation for the fitted value of $\langle \mathcal{P}_\tau \rangle$. The hatched area is background and the dashed and dotted lines correspond to the positive and the negative polarisation contributions respectively.

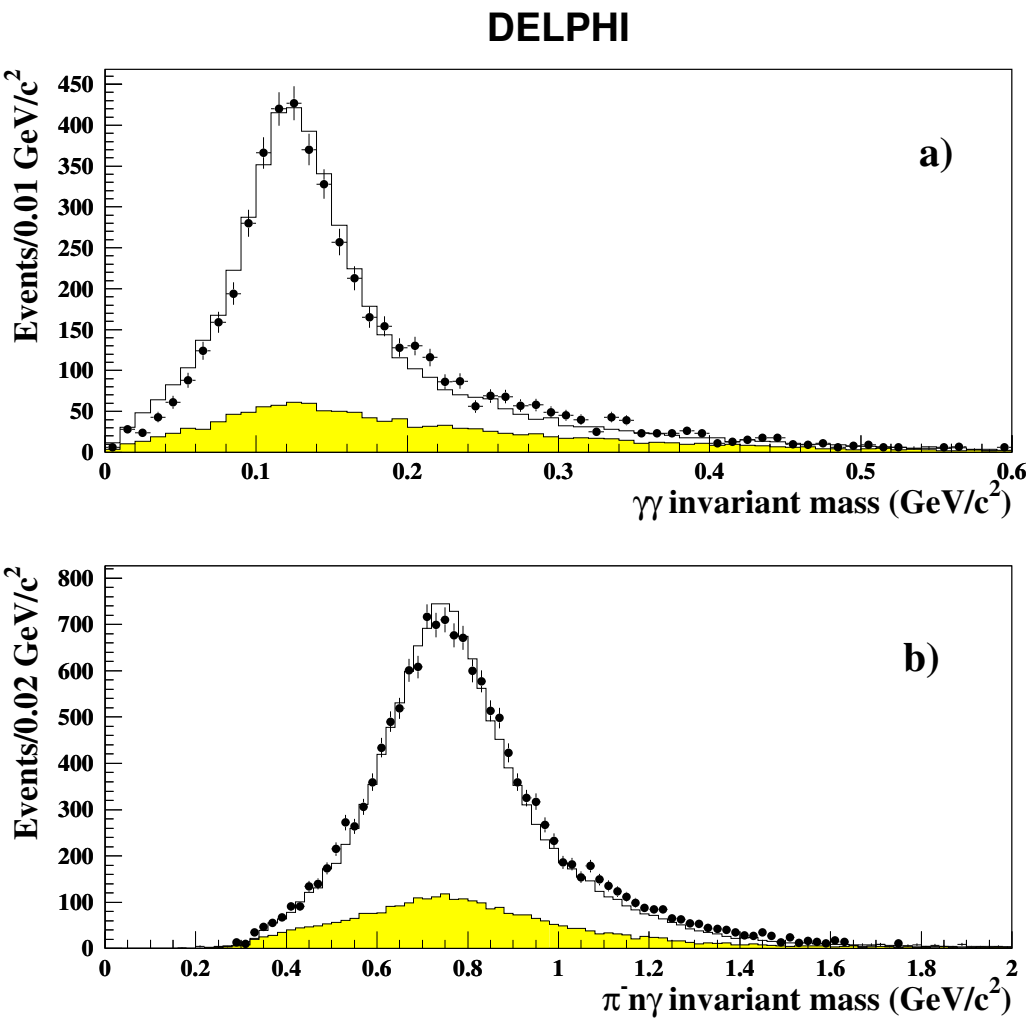

Figure 9: **a)** $\gamma\gamma$ and **a)** $\pi n\gamma$ invariant mass distribution for $\tau \to \rho\nu \to \pi\pi^0\nu$ candidate decays. The circles show the real data, the solid line simulation and the hatched area the background.

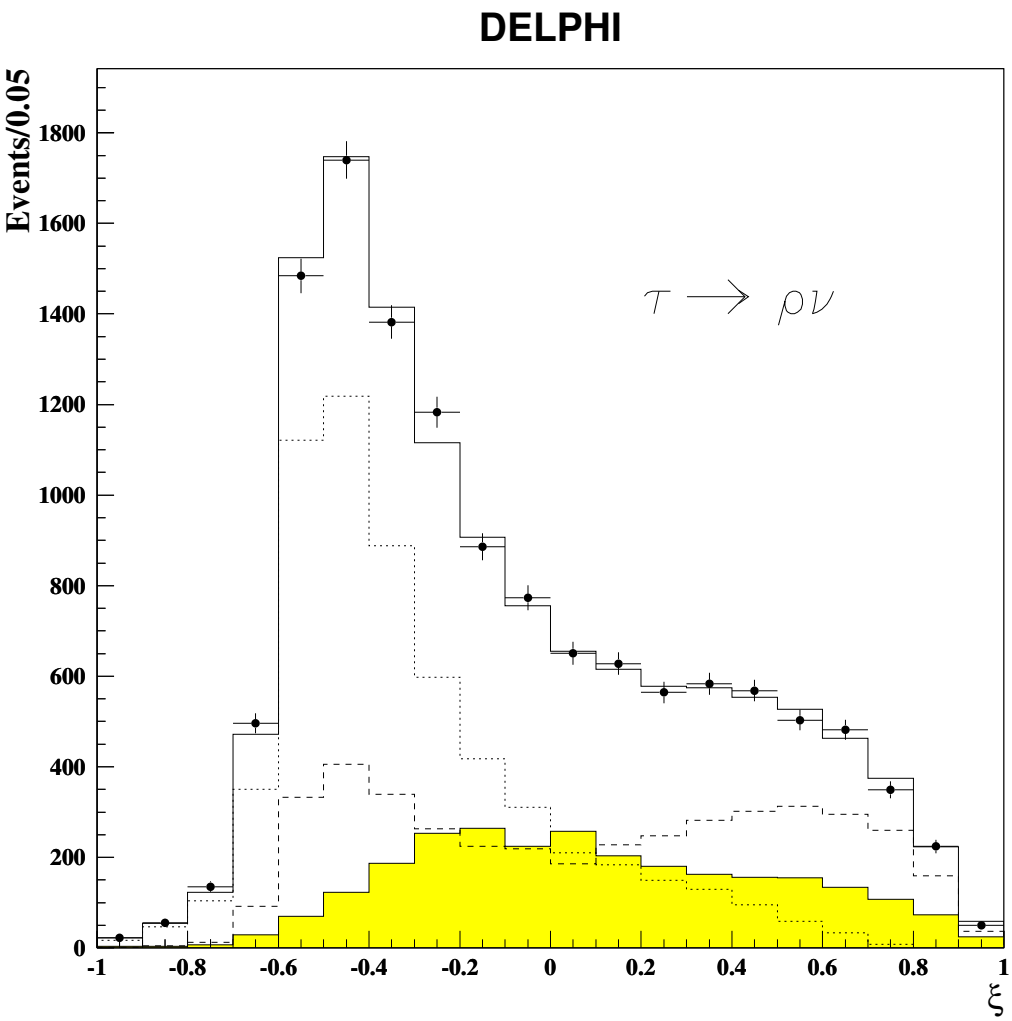

Figure 10: The observed ξ spectrum of candidate $\tau \to \rho\nu$ decays The circles are data and the solid line is simulation for the fitted value of $\langle \mathcal{P}_\tau \rangle$. The hatched area is background and the dashed and dotted lines correspond to the positive and the negative polarisation contributions respectively.

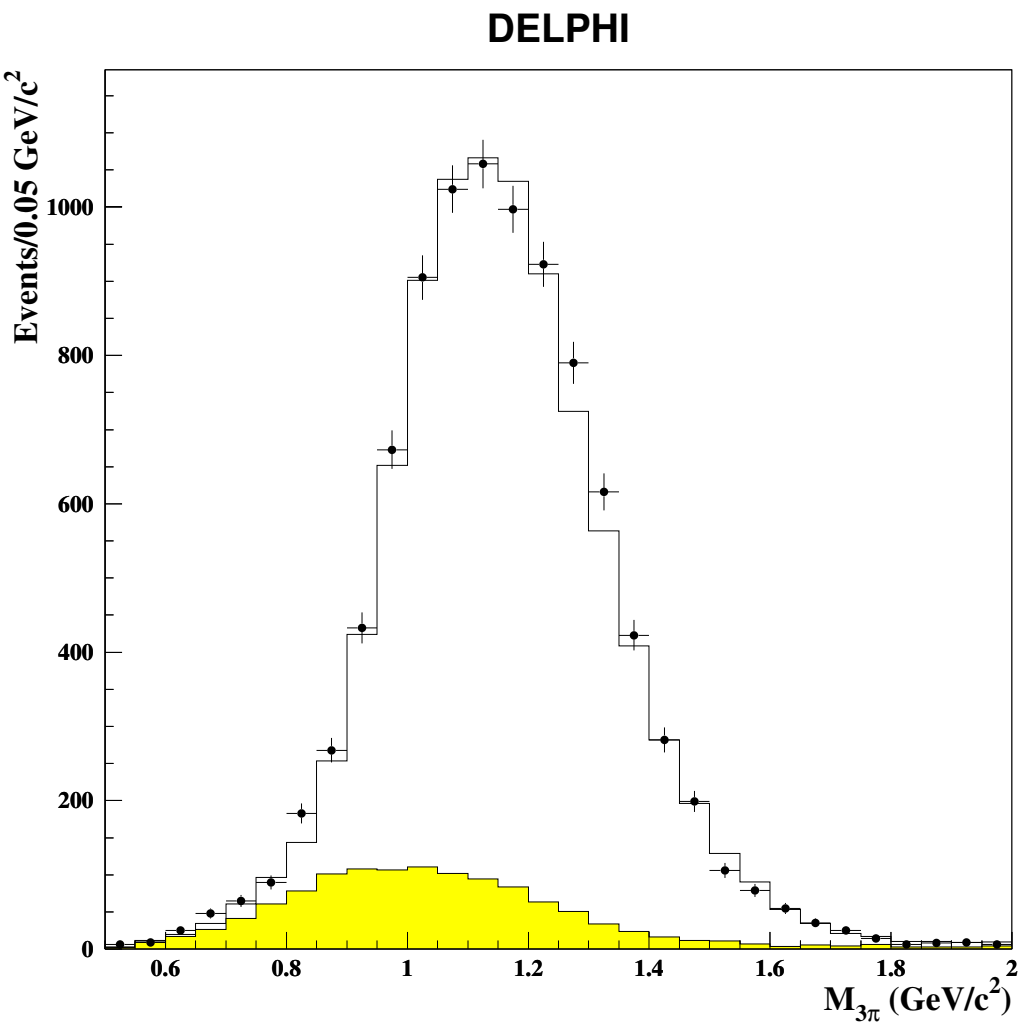

Figure 11: The 3π invariant mass spectrum from $\tau \to 3\pi^{\pm}\nu_{\tau}$ decays. The circles are data, the histogram corresponds to simulation and the hatched area is background.

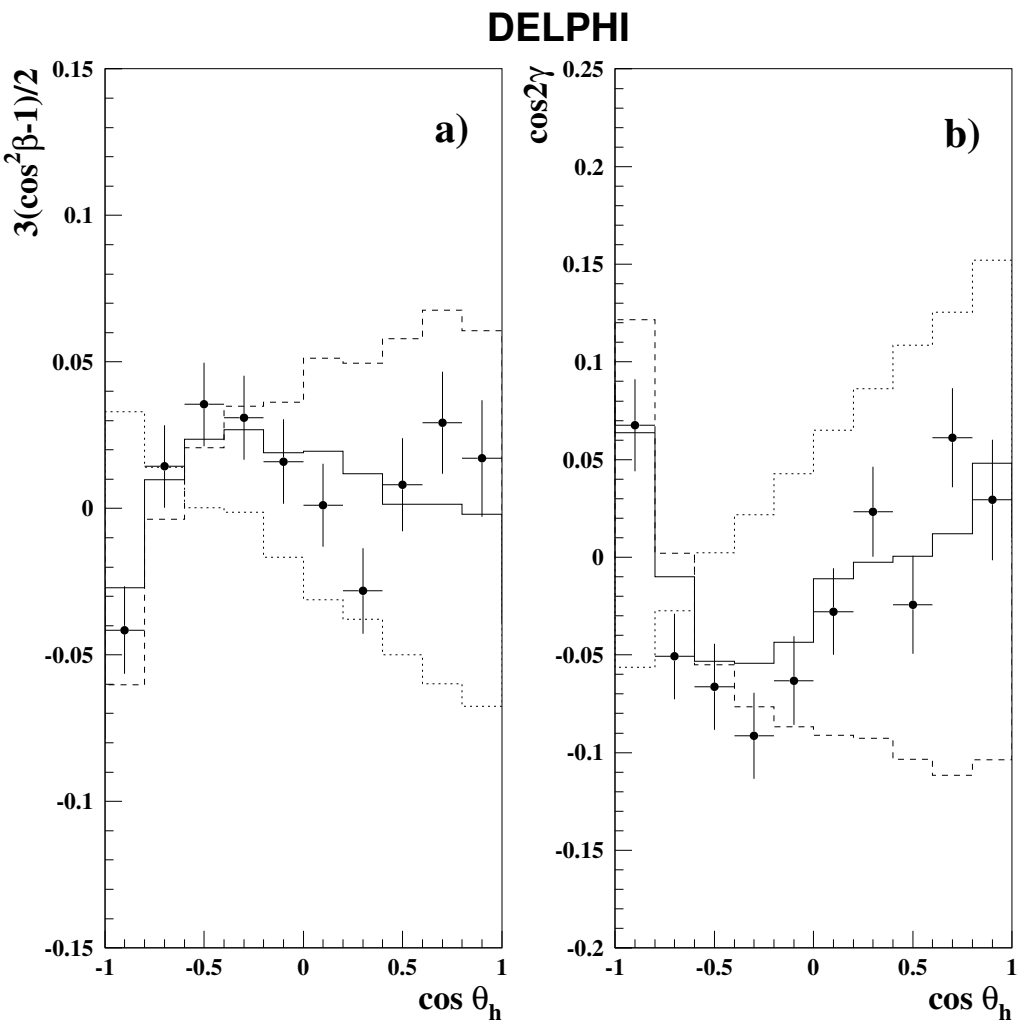

Figure 12: The two most sensitive moments in the polarisation fit of the $\tau \to \mathrm{a}_1\nu$ channel as a function of $\cos\theta_h$: **a)** $\langle(3\cos^2\beta - 1)/2\rangle$ and **b)** $\langle\cos 2\gamma\rangle$. The circles show the data and the solid line is simulation for the fitted value of $\langle\mathcal{P}_\tau\rangle$. The dashed and dotted lines correspond to the positive and the negative polarisation distributions respectively.

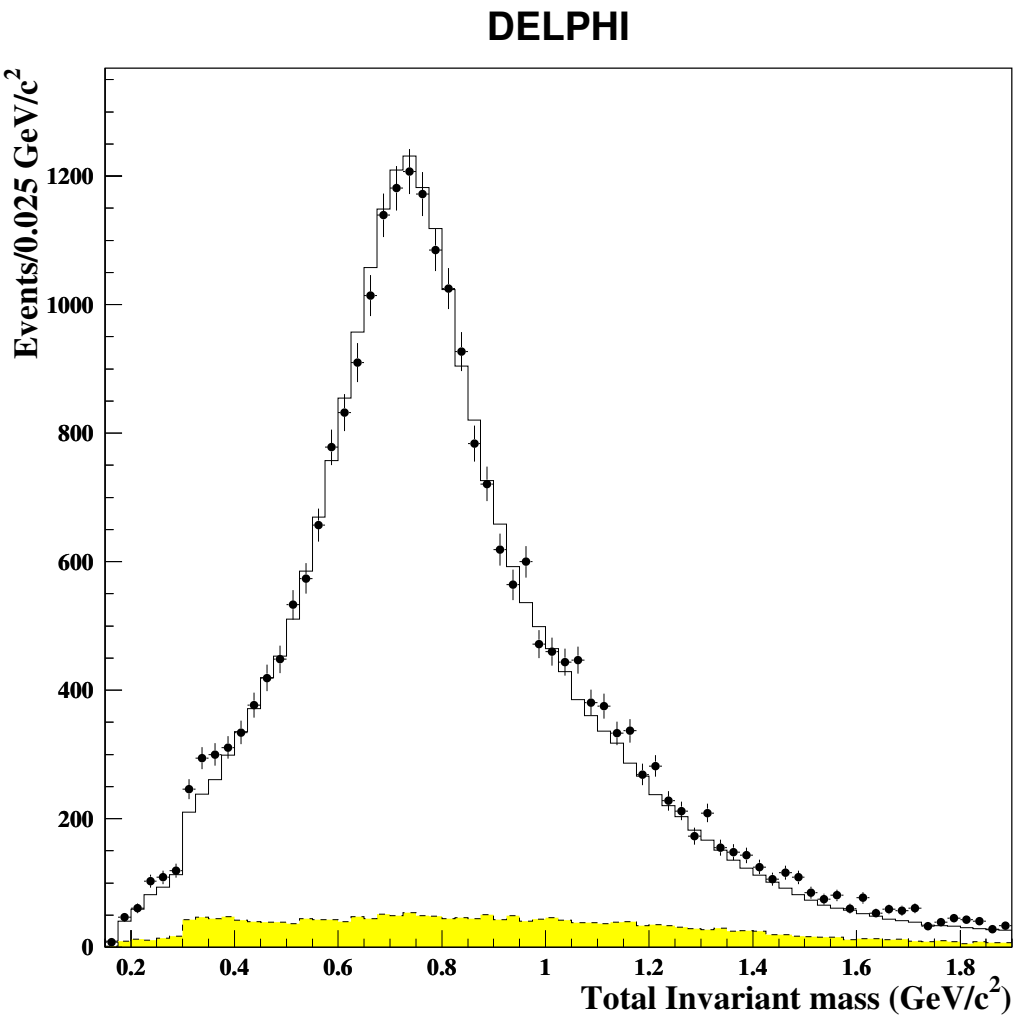

Figure 13: The observed invariant mass distribution for candidate events in the barrel in the one-prong hadron inclusive analysis. The circles are data, the solid line is simulation, and the hatched area represents the external background and all τ decays excepting the $\tau \to \pi(\mathrm{K})\nu$, $\tau \to \rho\nu$ and $\tau \to \mathrm{a}_1\nu$.

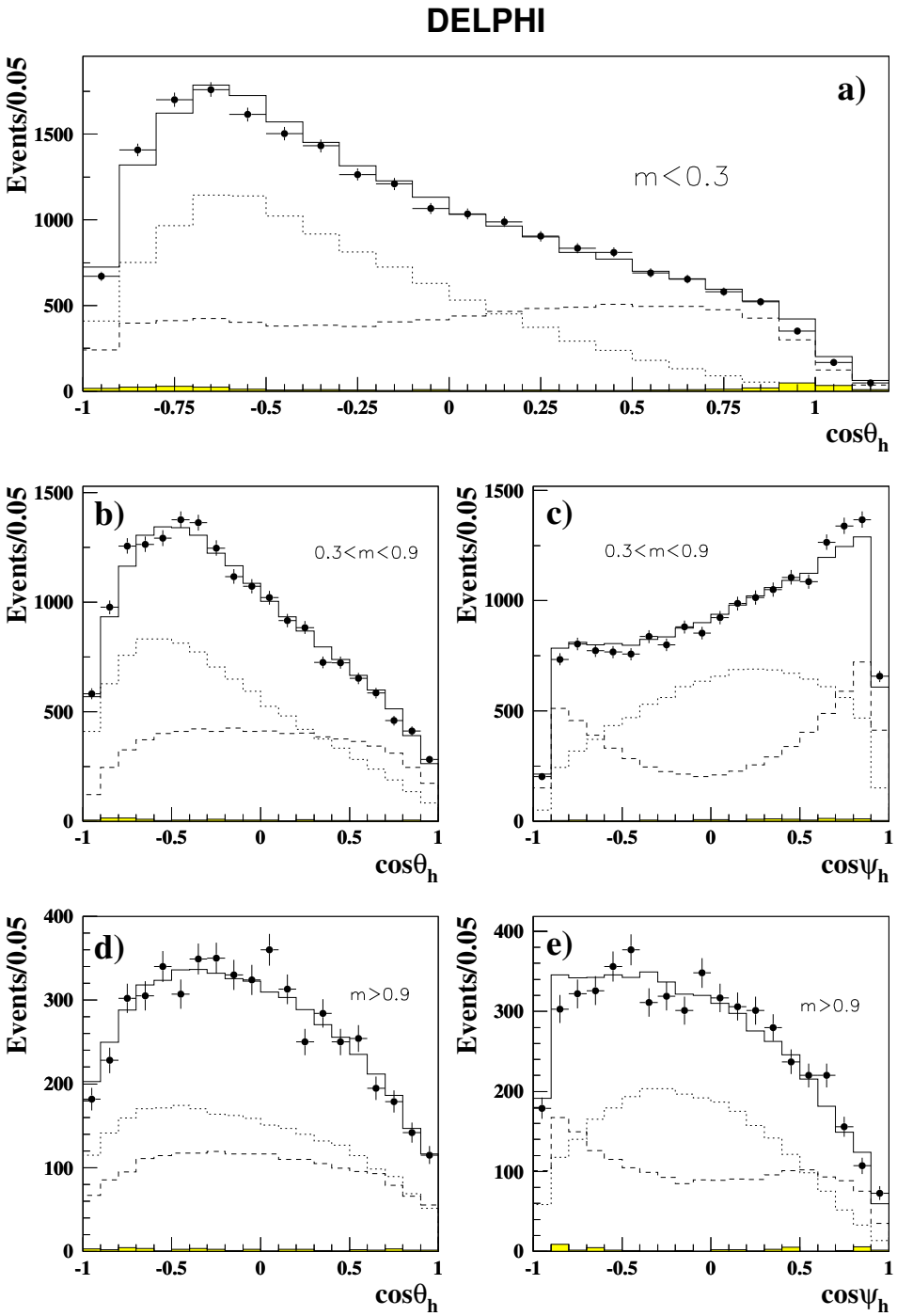

Figure 14: For the one-prong hadron inclusive analysis, the projections of the $\cos\theta_h$ vs $\cos\psi_h$ 2-dimensional distributions for the three invariant mass regions (only $\cos\theta_h$ for the first mass range, where $\cos\psi_h$ has no significance): **a)** $m_h < 0.3$ GeV/c^2; **b)** and **c)** 0.3 GeV/c^2 $< m_h <$ 0.9 GeV/c^2; **d)** and **e)** 0.9 GeV/c^2 $< m_h <$ 1.8 GeV/c^2; The circles are data and the solid line is simulation for the fitted value of $\langle \mathcal{P}_\tau \rangle$. The hatched area is background and the dashed and dotted lines correspond to the positive and the negative polarisation contributions respectively.

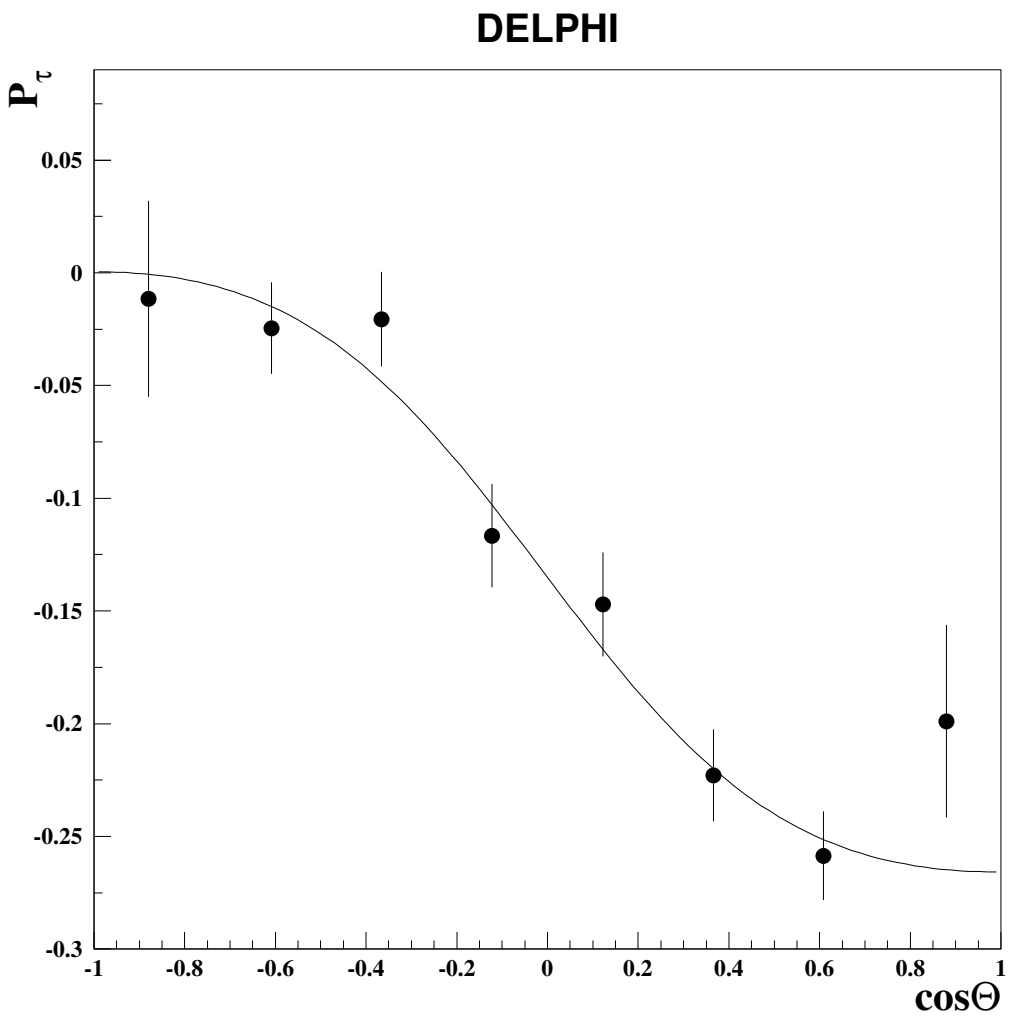

Figure 15: Data points show measured $\mathcal{P}_\tau$ as a function of cosΘ. The full curve represents theoretical expectation for the fit result.